

## 14. HETEROGENEITY OF OCEANIC PERIDOTITE FROM THE WESTERN CANYON WALL AT MARK: RESULTS FROM SITE 920<sup>1</sup>

Christopher J. Stephens<sup>2</sup>

### ABSTRACT

Drilling on the western canyon wall of the Mid-Atlantic Ridge south of the Kane Fracture Zone (23°N at MARK) penetrated 200 m into serpentinized spinel peridotite exposed in the footwall of a low-angle, east-dipping, normal fault system. A total penetration of 320 m was achieved in two holes (Holes 920B and 920D), from which recovery averaged approximately 48%. This degree of recovery is unique in sampling of oceanic peridotite. These holes thus represent an opportunity to examine not only the mineralogical and bulk composition of in situ oceanic peridotite, but also the degree and character of any heterogeneity in those parameters.

Mineral compositions in peridotite are remarkably uniform, considering the large apparent modal heterogeneity. The peridotites were classified during shipboard studies as predominantly harzburgite and orthopyroxene-rich harzburgite (orthopyroxene ranging up to 35 modal%) with volumetrically minor dunite and lherzolite. Mg numbers in olivine and orthopyroxene average 90.7, consistent with the peridotites being moderately depleted in terms of the previously identified, regional variation in North Atlantic oceanic peridotite mineralogy. Chrome spinel is correspondingly  $\text{Al}_2\text{O}_3$ -rich ( $\text{Cr}/[\text{Cr} + \text{Al}] \sim 28$ ), and orthopyroxene contains moderate  $\text{Al}_2\text{O}_3$  and  $\text{Cr}_2\text{O}_3$  contents.

Trace-element analyses of whole-rock samples using inductively coupled plasma mass spectrometry indicate that "background" peridotites have very low abundances of high-field-strength elements, with  $\text{Y} < 1 \text{ ppm}$  and  $\text{Zr}$  averaging about 60 ppb.  $\text{Nb}$  and  $\text{Ta}$  abundances are less than ~30 ppb, and typically are <10 ppb. Chondrite-normalized rare-earth element (REE) patterns show strong depletions in light rare-earth elements ( $\text{LREE} < 10^{-3}$  times chondrite). REE abundances in the most depleted compositions are consistent with the harzburgite forming the residue to 15% to 20% fractional melting, approaching clinopyroxene exhaustion, of a fertile lherzolite. Erratic enrichment in LREE that is not reflected in changes in mineral major-element chemistry is consistent with selective enrichment of the peridotites by a fluid rich in LREE and, to a lesser extent,  $\text{Zr}$ . Selective enrichment is suggested to have accompanied the infiltration of melt through the peridotite, although textural or mineral chemistry evidence for melt infiltration is not preserved.

### INTRODUCTION

The mineralogy and composition of peridotites collected from seafloor exposures at mid-ocean ridges must reflect an integrated history of melt/mantle reaction during ascent of the mantle column. Current models for mantle uplift below zones of seafloor spreading (Klein and Langmuir, 1987; Langmuir et al., 1993; McKenzie and Bickle, 1988; Forsyth, 1993) suggest that the uplift history should be relatively similar for any localized mid-ocean ridge segment, but may vary significantly along the length of a ridge on the scale of as little as tens of kilometers.

There are differences of degree attributed to factors affecting the degree of melt extraction during upwelling, depending on whether the model is an active or passive one. The primary influences on the degree of melt extraction, however, are differences in the mantle potential temperature, expressed as the geothermal gradient (Klein and Langmuir, 1987), and differences in the uplift history as a function of the rate of spreading (Forsyth, 1993), which influences the amount of heat loss through conduction. Both of these factors can vary from place to place, but also over time at any one location, such that the geochemical evolution of any mantle sample reflects an integrated, dynamic history of upwelling.

Away from spreading centers, the thickness and depth below sea level of oceanic crust are independent of spreading rate, and can be

modeled in terms of thermal models for cooling crust as a function of age (Parsons and Sclater, 1977). Modeling of the elevation profiles over spreading centers, however, (Parsons and Sclater, 1977; Klein and Langmuir, 1987) shows that, at least for other than very slow spreading ridges, the depth below sea level to the top of the ridge can be modeled to the first approximation in terms of variations of the upper mantle temperature, both with depth and laterally away from the ridge. These observations suggest that, in terms of magmatic production and the resultant ridge and ocean-floor physiography, mid-ocean ridges respond relatively rapidly to minimize the effects of changes in upwelling dynamics. The question posed here is whether these changes result in mineralogical and geochemical heterogeneity in underlying mantle that has been subjected to changes in rates of processes during its history of upwelling.

In addition to the effects of melt extraction, the composition of lithospheric mantle is able to be modified by the addition of melt in varying ways. The bulk composition of peridotite can be modified by the incorporation of residues after closure of pathways during melt passage (Dick, 1989; Elthon, 1992; Takahashi, 1992; Hess, 1993). At levels above the peridotite solidus, there is likely to be insufficient heat to reequilibrate these residues, and they may retain their coherence as petrographically recognizable segregations. Dick (1989) argued that the abundance of plagioclase as a modal component in oceanic peridotite reflected melt infiltration and the capture of residual melt during vein closure.

At depths corresponding to the lithosphere, however, there may be sufficient latent heat and dynamic stress for melt pods to reequilibrate with the surrounding peridotite although such pods may remain, at least for a short time, as chemically enriched zones. Recognition of these pods may be difficult, although olivine websterite retrieved by

<sup>1</sup>Karson, J.A., Cannat, M., Miller, D.J., and Elthon, D. (Eds.), 1997. *Proc. ODP, Sci. Results*, 153: College Station, TX (Ocean Drilling Program).

<sup>2</sup>Department of Earth Sciences, The University of Queensland, Brisbane, 4072, Australia. Present address: School of Geology, Queensland University of Technology, 2 George Street, Brisbane, 4000, Australia. stephens@earthsciences.uq.edu.au

Dick et al. (1984) from dredge hauls in the MARK area and clinopyroxene-rich pods such as those observed in Cores 153-920D-13R and 15R (Kempton and Stephens, this volume) may be examples of this process occurring.

It is now widely argued that geochemical effects of mantle-derived refertilization processes, which do not require the capture of a melt fraction, can be observed in a range of ophiolitic, oceanic, and alpine-type peridotites (Navon and Stolper, 1987; Bodinier et al., 1990; Cannat et al., 1990; Elthon, 1992; Takazawa et al., 1992). Evidence for this enrichment lies principally in the interpretation of concave-upward, chondrite-normalized, rare-earth-element (REE) patterns in whole-rock and clinopyroxene analyses, although Elthon (1992) cited evidence in the anomalous Na<sub>2</sub>O abundances in oceanic peridotite when compared with compositions calculated from fractional melting models (Johnson et al., 1990). Hekinian et al. (1989) argued for the existence of mantle heterogeneity on the basis of variations in the chemistry of off-axis basalts from the East Pacific Rise.

There is thus considerable conjecture as to the scale of interactions that occur below mid-ocean ridges in terms of melt extraction and subsequent selective or bulk mass addition during upwelling. On a regional scale, the averaged variations in mineral, modal, and calculated bulk peridotite major- and trace-element compositions are shown to be consistent with melt extraction under a combination of passive and dynamic factors (Dick et al., 1984; Michael and Bonatti, 1985; Klein and Langmuir, 1987; Forsyth, 1993). Hess (1993), Niu and Batiza (1993), and Niu et al. (1995), nonetheless, have pointed out that crystallization of olivine is an inevitable consequence of adiabatic melt migration to shallower depths, and this should be reflected in modal chemistry. Good correlations between bulk chemistry and trace-element chemistry on a local scale should support simple models of fractional melting during upwelling as the major interaction between mantle and melt, whereas poor correlations may support models invoking widespread refertilization.

Onboard investigations argued for the modally heterogeneous nature of the Site 920 peridotite, suggesting that the peridotite had undergone a complex history of melt extraction (Shipboard Scientific Party, 1995). This paper presents mineral chemistry for 30 samples plus modal, whole-rock major- and trace-element data for 21 samples of peridotite from Site 920. The relation between these data sets is explored, and the trace-element data are used to argue for the peridotite having been impregnated with a fluid enriched in light REE (LREE), for which there is no observed petrographic or major-element expression.

## ANALYTICAL DATA

Samples for this study were collected throughout Holes 920B and 920D (Fig. 1) with the aim of sampling as wide a range of modal compositions as possible. As a result, the data presented here cannot be considered volumetrically representative of the peridotite mass drilled. Onboard studies (Shipboard Scientific Party, 1995), nonetheless, showed that harzburgite with 10 to 20 modal% orthopyroxene was the overwhelmingly abundant rock type, with very minor lherzolite and dunite. Although the samples analyzed here generally reflect this pattern, no attempt has been made to infer that the bulk average of these compositions accurately reflects a bulk average for the Mid-Atlantic Ridge south of the Kane Fracture Zone (MARK) area. The same constraints should also be seen as applying to results of other studies referenced in this paper.

Modal data is widely regarded as difficult to collect for oceanic peridotites because of their coarse-grained, porphyroclastic texture (Dick et al., 1984), generally high degree of serpentinization, and problems relating to sample size. Dick et al. (1984) and Michael and Bonatti (1985) have, nonetheless, argued that pseudomorphic textures in serpentinite are faithful reproductions of the primary mineralogy and mineral modes.

Modal data quoted here are based on similar petrographic criteria to those studies. The author's observations support the findings of those authors in that, except in localized deformation zones, there is no petrographic evidence for strain having developed because of volume changes either associated with, or after, serpentinization. Although the criteria for the distinction of orthopyroxene from clinopyroxene is regarded as difficult in heavily serpentinized rocks, there appeared to be a clear petrographic distinction in the samples examined. Clinopyroxene pseudomorphs were recognized by the presence of coarse, oxide-rich, exsolution lamellae and strain twinning, and by the tendency for the grains to have coarse, interstitial (holly leaf), textural relationships. Pseudomorphs after orthopyroxene are typically recognizable by the even replacement of relatively coarse grain sizes by bastite. Olivine pseudomorphs reflect equant subgrain textures with radial serpentine textures within subgrains and high abundances of fine-grained magnetite production. Crosscutting veins of serpentine were excluded from modal counts.

Given the sampling constraints on both size of sample and Ocean Drilling Program (ODP) policy with regard to core holes, the estimation of modal compositions from core samples (typically ~50 cm<sup>3</sup> as 50 × 25 cm quarter cores or 40 × 57 cm slabs cut from the half core face) is a somewhat more acute problem than from samples acquired by dredging, the most common method by which oceanic peridotite has been retrieved in the past. In this study, modal compositions were calculated after measuring 2000 points per sample on standard 25 × 50 mm (12.5 cm<sup>2</sup>) polished sections cut predominantly from quarter cores. This point density was chosen to provide an accurate map of each section, including chrome spinel, which has a grain-size range of 0.1–2 mm.

Despite attempts to minimize errors in the modal estimates, the data presented here should be interpreted with some caution, given ambiguities in both the assignment of the mineral type and in the problem of thin-section size and orientation. The sampling density compares favorably with the 400 points per 8 cm<sup>2</sup> measured by Michael and Bonatti (1985), although less favorably with the 2400 points per 24 cm<sup>2</sup> measured by Dick et al. (1984). Both of those studies examined data from dredge samples collected from sites on the Mid-Atlantic Ridge and Indian Ocean ridge systems, and data for each locality were presented as averaged data for all of the measured samples from each site. This approach reflected the regional nature of those studies, and the number of measured samples from any one site ranged from 1 to 16 samples although, in both studies, the most common number of samples was between 1 and 7.

Mineral compositions were measured by wavelength-dispersive spectrometry using a four-channel JEOL JXA-8800L Superprobe housed at the Centre for Microscopy and Microanalysis at The University of Queensland. Counting times were chosen to achieve better than 0.5% standard deviation across the range of analyzed elements for measured abundances greater than 1%. The procedure was standardized against a combination of natural and synthetic standards (Table 1), and results were calculated with the proprietary JEOL ZAF correction routine.

Olivine and spinel compositions were measured using the minimum beam diameter (nominally 1 μm for a ~2- to 2.5-μm-diameter source volume). Traversing of grains did not detect core-rim variations that could be ascribed to primary compositional variations. Pyroxene grains were measured using both minimum and 15-μm-diameter beam sizes. Expanding the beam diameter to 15 μm did not significantly reduce the effects of compositional variation caused by low temperature exsolution of the corresponding orthopyroxene or clinopyroxene, which occurs on the scale that varies from finer than the resolution of the scanning electron microscope (<1 μm) to several microns. Note that the configuration of the JEOL Superprobe is such that the counting windows are exposed to only a 10-μm-wide and 40-μm-long window on the sample, and that using beam diameters greater than ~15 μm will compromise the accuracy of the measurement.

Although strictly flawed in principle, expansion of the beam diameter, sometimes to diameters of 100 μm or more, is widely used as

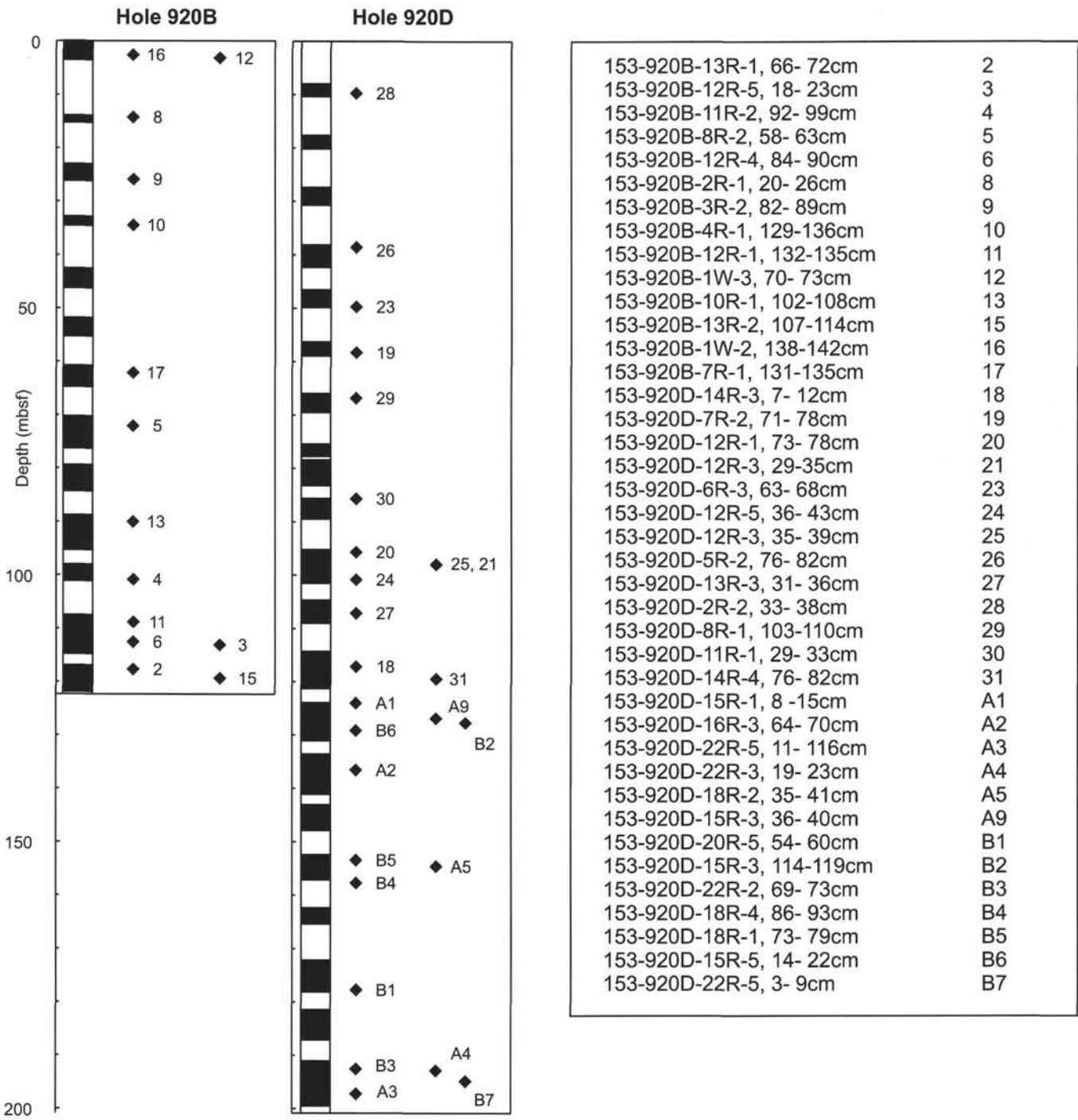


Figure 1. Distribution of samples studied in this paper relative to the recovery (black columns to the left of each hole) for Holes 920B and 920D. Table on right defines sample codes used on figure.

a technique of averaging out the compositional segregation caused by exsolution in pyroxene. In terms of the technique, this approach relies on the assumption that the variation in the absorption of source volume seen by spectrometers is insignificant at the scale measured. Although this may be a reasonable assumption for orthopyroxene and clinopyroxene, there may be errors caused by the different ray paths seen by different spectrometer orientations relative to the orientation of the lamellae. In a geological sense, the technique relies on the inference that the redistribution of elements during low-temperature, subsolidus equilibration is limited within the host grain. As a result, it is common practice to only analyze cores of exsolved grains, al-

though this can be difficult, especially for clinopyroxene, where the grain size is not large. Dick et al. (1984) applied a different approach in hand-picking grains of pyroxene and fusing them prior to analysis.

Both of these practices are arguably effective in achieving the aim of characterizing the higher temperature and pressure composition of the mineral. Lamellae-free margins to pyroxene grains clearly indicate that migration of cations up to the range of 1 mm occurs. The effect of exsolution on pyroxene analyses during this study was to give a wide range of CaO contents, and hence wollastonite (Wo):enstatite (En) ratios, for any set of analyses. Nonetheless, the contained weight percentages of oxides commonly regarded as significant in petroge-

**Table 1.** Operating and calibration conditions for microprobe analysis of mineral phases in peridotite from Holes 920B and 920D.

Element	Crystal	Channel	Standard
Si	TAP	3	Wollastonite.t
Ti	PET	2	TiO <sub>2</sub> .t
Al	TAP	3	Lake County Plagioclase
Cr	PET	2	Chromite.t
Fe	LIFH	4	Fe <sub>2</sub> O <sub>3</sub> .t
Mn	LIFH	4	Spessartine.t
Ni	LIFH	4	Ni Olivine
Mg	TAP	3	MgO.t
Ca	PET	2	Wollastonite.t
Na	TAP	1	Amelia Albite.t
K	PET	2	Orthoclase.t

Notes: LIFH refers to LIF mounted on high Rowland Circle spectrometer. Standards denoted as ".t" indicate standards mounted on George Taylor Block. Accelerating potential was 15 kV, and the beam current was 15 nA. Na and K were standardized using a 10-μm beam diameter.

netic studies of residual pyroxenes (e.g., Al<sub>2</sub>O<sub>3</sub> and Cr<sub>2</sub>O<sub>3</sub>) varied sympathetically, and independently of CaO (Figs. 2A, 2B), suggesting that any of the generally practiced methods of averaging would not enhance the quality of the data. Nonetheless, coarse lamellae were avoided during measurement, and analyses in which CaO was <19.5% for clinopyroxene and >3% in orthopyroxene were excluded from the data reduction. The data are presented here as averages for individual samples, and are based on between 1 and 27 analyses from each sample.

Powders for major- and trace-element analysis were prepared by grinding all surfaces to cleanliness using silicon carbide powder on glass plates to remove any contamination resulting from contact with drilling or cutting apparatus. Blocks were then washed in alcohol and Milli-Q water in an ultrasonic bath to remove any organic or particulate contaminants. Large blocks were broken down in a carbon-steel percussion mill prior to pulverizing in a hardened steel TEMA mill. Checks on this method of preparation indicate that contamination in hard media (quartz) is restricted to less than 350 ppb Sc, V, and Co, and approximately 2.5 ppm Cu, levels far below the natural abundances in these rocks (>4 ppm). Contamination of Nb and Ta is at the 1 to 3 ppb detection level, which, although comparable in absolute levels to some of the analyzed peridotites, is regarded as a maximum, given the differences in hardness of quartz relative to serpentinized peridotite.

Whole-rock major-element, Ni and Cr abundances were analyzed on a Phillips PW140 XRF, and other trace elements were analyzed on a Fisons Quadrupole inductively coupled plasma mass spectrometer (ICP-MS), at the Department of Earth Sciences, The University of Queensland. The ICP-MS is housed in a high-quality clean laboratory with trace-element blank levels less than 0.1 ppb. Analytical quality was monitored against the international standards BIR-1 and PCC-1.

Note that in both major- and trace-element analyses, dissolution of chrome spinel remains an ongoing problem that is not yet resolved. The consequences of this in terms of analyses are not yet fully understood. It is unlikely to significantly effect Al<sub>2</sub>O<sub>3</sub> contents, given the low modal abundances of spinel, but Nb and Ta abundances may be affected. There is, nonetheless, no evidence to suggest that the Nb/Ta ratio may change as a result of their incomplete dissolution, and the interpretations reported here are not considered to be compromised by this problem.

## RESULTS

Modal data for 21 MARK peridotites (Table 2) suggest that they are predominantly harzburgite, averaging 82.5 modal% olivine + serpentine, 15.3% orthopyroxene, 2.1% clinopyroxene, and 1% chrome spinel. This average contains significantly more olivine (cf. 75%),

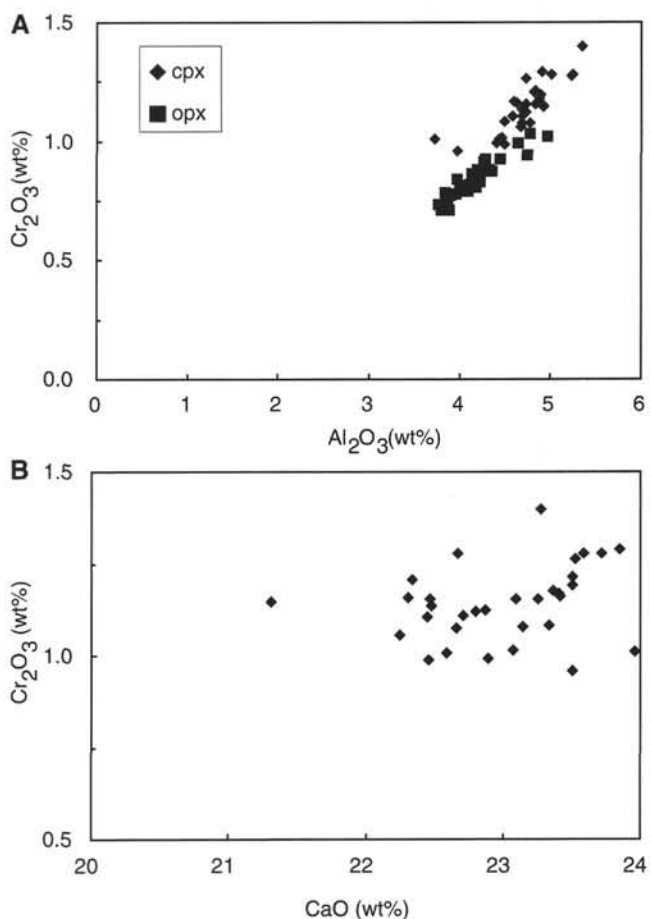


**Figure 2.** A. The distribution of Al<sub>2</sub>O<sub>3</sub> and Cr<sub>2</sub>O<sub>3</sub> in average microprobe analyses of clinopyroxene and orthopyroxene from Site 920. Note the expected good correlation and slightly lower abundances of both elements in orthopyroxene. B. Cr<sub>2</sub>O<sub>3</sub> vs. CaO in clinopyroxene. Note the poor correlation. These graphs together indicate that orthopyroxene exsolution does not degrade microprobe analyses for minor elements despite the obvious effect on the ternary pyroxene components.

and perhaps spinel (cf. 0.5%), relative to the average of oceanic peridotite samples computed by Dick et al. (1984). This suggests that Site 920 peridotites are mineralogically depleted compared with the Atlantic-Indian average oceanic peridotite. Two samples are modally estimated as lherzolite and three samples as dunite, the latter being completely serpentinized except for trace abundances of spinel. The degree of serpentinization ranges from 35% to 100% for silicate minerals.

The typical texture of the peridotites is porphyroclastic, defined by elongate orthopyroxene grains up to 1.5 cm in length (Shipboard Scientific Party, 1995). Fresh olivine is found as subgrain aggregates surrounding the orthopyroxene grains and, where unaltered, forms an equigranular subgrain mosaic after parent grains up to 3 mm in size. Given the ease with which olivine recrystallizes, these parent grain sizes are unlikely to have any significance. Clinopyroxene forms interstitial grains that rarely exceed 2 mm in size. Chrome spinel ranges in color from deep brown to honey brown, and ranges from 0.1 to 2 mm in size. Clinopyroxene and spinel commonly occur as trails cutting across the porphyroclastic fabric. Trace amounts of nickel sulfide and pyrite, the latter probably introduced during serpentinization, were observed.

Despite the apparent modal heterogeneity of the Site 920 peridotite, there is no determinable variation in mineral composition either with modal composition or across the range of measured composi-

**Table 2.** Modal compositions of peridotite from Holes 920B and 920D.

Core, section, interval (cm)	Serpentinization	Olivine	Orthopyroxene	Clinopyroxene	Spinel
<b>153-920B-</b>					
13R-1, 66–72	79.40	2.00	16.90	1.20	0.50
12R-5, 18–23	71.50	22.40	1.70	0.90	3.50
12R-4, 84–90	84.20	0.00	9.40	6.30	0.10
2R-1, 20–26	67.10	4.00	28.50	0.00	0.40
12R-1, 132–135	99.70	0.00	0.00	0.00	0.30
10R-1, 102–108	82.20	0.80	15.80	0.00	1.20
7R-1, 131–135	100.00	0.00	0.00	0.00	0.00
<b>153-920D-</b>					
14R-3, 7–12	35.10	41.50	17.80	5.10	0.50
12R-3, 29–35	79.00	4.80	14.10	1.20	0.90
12R-5, 36–43	100.00	0.00	0.00	0.00	0.00
12R-3, 35–39	79.30	2.30	15.10	2.50	0.80
5R-2, 76–82	83.20	0.00	12.10	2.70	2.00
2R-2, 33–38	82.40	3.90	11.70	0.70	1.30
14R-4, 76–82	47.00	23.30	26.10	3.20	0.40
15R-1, 8–15	61.00	9.40	26.60	2.40	0.60
16R-3, 64–70	70.40	8.20	16.60	3.50	1.30
22R-5, 11–116	76.80	1.30	18.60	2.20	1.10
18R-2, 35–41	73.60	0.90	24.20	0.60	0.70
22R-2, 69–73	76.80	13.00	4.45	3.65	2.10
15R-5, 14–22	79.60	6.50	10.30	2.50	1.10
22R-5, 3–9	51.90	7.80	36.60	3.20	0.50

tions for the Site 920 peridotites. Olivine compositions are extremely consistent, typically 0.36%–0.40% NiO, and have consistent Mg numbers ( $Mg\# = Mg/\Sigma[Mg + Fe]$ ) of  $90.7 \pm 0.5$  (Table 3). Pyroxene compositions are indistinguishable in terms of their principal components (Fig. 3; Tables 4, 5); orthopyroxene has Mg# values similar to coexisting olivine, and clinopyroxene has consistently higher Mg# around 93. Chrome spinel (Table 6) has Cr# ( $Cr/\Sigma[Cr + Al]$ ) values about 28, and shows a limited range of 25 to 29 (Fig. 4). Not surprisingly,  $Al_2O_3$  and  $Cr_2O_3$  in pyroxene are well correlated, with slightly higher values of both oxides in clinopyroxene. Cr# values in clinopyroxene and orthopyroxene are, nonetheless, relatively constant at 0.140 and 0.115, respectively.

The Site 920 data were plotted in terms of components sensitive to the degree of melt extraction (Mysen and Kushiro, 1977; Jacques and Green, 1980) vs. the Mid-Atlantic Ridge data set of Michael and Bonatti (1985) in Figure 4. The Site 920 data consistently plot in the middle of the range on all plots, suggesting that the Site 920 peridotites are “moderately depleted” in a regional sense. This contrasts with the modal data that suggest the Site 920 peridotites are olivine rich, and hence modally depleted relative to Mid-Atlantic Ridge and Southwest Indian Ridge peridotites.

## GEOCHEMISTRY

### Major Elements

Comparison of major-element data (Tables 7, 8) based on calculated compositions of peridotites is clearly complicated by the inherent inaccuracy in estimating modes and in the accuracy of analysis of minor elements in pyroxene by electron microprobe. A comparison of the measured and calculated MgO contents for 20 Site 920 peridotites shows this (Fig. 5A), illustrating not only that the calculated MgO content is dominated by the, perhaps inaccurate, estimated modal olivine content, but also that measured compositions are significantly more homogeneous in MgO, except for dunites.

This relative homogeneity is further illustrated by the tight clustering of the measured compositions in terms of their Mg-Al variations (Fig. 5B), which should reflect the depletion of aluminous pyroxene relative to olivine. The Site 920 data define a tight cluster, which reinforces that the modal estimates must be in error. Only two samples of dunite are clearly distinguished on this plot, emphasizing that the optical estimation of modes in grain-size-reduced and serpentinized peridotites must be undertaken with caution.

The measured Site 920 compositions are comparable with calculated compositions for American-Antarctic Ridge/Southwest Indian

Ridge peridotites from the Bullard and Islas Orcadas Fracture Zones (Table 7, 8), consistent with the relative compositions of the mineral phases. They are clearly less depleted in pyroxene than samples from 43°N (Fig. 5B), consistent with the inferred higher degrees of depletion of the 43°N peridotite from their high Cr# in spinel (45 to 55; Shibata and Thompson, 1986).

### Trace Elements

Trace-element analyses (Table 9) were obtained on rock types modally categorized as ranging from dunite to lherzolite. Of the large-ion-lithophile elements, Rb abundances are variable, ranging from 6 to 110 ppb. Ba shows a large range of abundances, from 43 to 702 ppb, which probably reflects serpentinization and addition from seawater, as evidenced by a relatively strong correlation with Cs (Fig. 6A). Sr is generally constant at 2–4 ppm except for one anomalous sample containing 98 ppm that was found to contain a spinel-plagioclase veinlet. Sr/Zr ratios show a relatively good correlation with Zr, defining two populations of different negative slope and inflection at about 60 ppb Zr (Fig. 6B). The significance of this correlation is unclear, but it is unlikely to be reflecting the introduction of Sr in seawater given the correlation with a high-field-strength element (HFSE).

The abundances of HFSEs are variable: Zr ranges from about 30 to 200 ppb, and Y from 320 to 720 ppb. Nb abundances are very low, ranging from 2 to 14 ppb and thus approach the levels of depletion occurring in some of the most depleted island-arc systems (e.g., the Lau-Tonga arc system; A. Ewart unpubl. data). HFSE abundances correlate poorly both with each other and with REE, suggesting that the processes effecting their abundances are not systematic. Ta abundances are very low (most samples have less than 10 ppb Ta), but range up to 24 ppb. Although the precision of these values is excellent, the accuracy is questionable because there is no systematic behavior in Nb/Ta ratios. Zr/Hf ratios vary systematically from values of 5 up to about 25 as Zr increases from about 30 to 196 ppb (Fig. 6C).

The analyses can be organized according to their REE patterns into four different groups (Fig. 7). A group of LREE-depleted samples patterns shows moderately negative-sloping, chondrite-normalized patterns for the heavy REEs (HREEs), Eu, and Sm, and steep patterns with negative slopes for the elements La–Nd. HREE abundances range from 0.1 to 1× chondrite, and  $Sm_N$  and  $Eu_N$ , from 0.7 to 0.9 (LREE-depleted group; Fig. 7A). La and Ce are below the detection limit of the ICP-MS (1–3 ppb) for most of the samples within this group. A notable feature of this group is the sudden depletion in

**Table 3. Average olivine compositions for peridotites from Site 920.**

Hole:	153-920B	153-920D	153-920D	153-920D	153-920D	153-920D	153-920D										
Core, section:	13R-1	12R-5	12R-4	13R-2	2R-1	3R-2	4R-1	1W-3	10R-1	12R-5	13R-2	14R-3	7R-2	12R-1	12R-3	6R-3	12R-3
Interval (cm):	66–72	18–23	84–90	114–120	20–26	82–89	129–136	70–73	102–108	23–28	107–114	7–12	71–78	73–78	29–35	63–68	35–39
n:	7	5	2	11	4	1	9	7	9	4	10	18	13	10	13	14	2
SiO <sub>2</sub>	41.44	41.08	40.78	40.88	41.72	41.48	41.84	41.12	41.49	41.50	40.88	41.20	41.42	41.60	41.07	41.43	41.25
TiO <sub>2</sub>	0.01	0.01	0.00	0.01	0.02	0.04	0.01	0.01	0.01	0.01	0.01	0.01	0.02	0.01	0.00	0.00	0.02
Al <sub>2</sub> O <sub>3</sub>	0.01	0.02	0.01	0.01	0.01	0.02	0.02	0.01	0.01	0.02	0.01	0.01	0.01	0.01	0.01	0.01	0.01
Cr <sub>2</sub> O <sub>3</sub>	0.02	0.02	0.03	0.01	0.11	0.00	0.02	0.02	0.01	0.01	0.01	0.01	0.01	0.01	0.01	0.00	0.01
FeO	9.03	9.12	9.20	8.99	8.60	9.08	8.94	9.14	9.17	9.27	9.04	9.36	9.29	9.27	9.06	9.15	9.25
MnO	0.13	0.12	0.14	0.13	0.14	0.17	0.14	0.14	0.14	0.14	0.13	0.13	0.13	0.13	0.13	0.13	0.12
NiO	0.36	0.38	0.37	0.37	0.39	0.38	0.39	0.38	0.38	0.38	0.38	0.37	0.40	0.37	0.39	0.38	0.35
MgO	50.13	50.22	48.82	49.05	50.49	50.55	50.45	50.29	50.40	50.37	49.30	49.92	50.43	50.51	49.38	50.28	50.08
CaO	0.05	0.04	0.05	0.02	0.04	0.05	0.03	0.03	0.03	0.04	0.02	0.04	0.02	0.03	0.02	0.03	0.03
Na <sub>2</sub> O	0.01	0.00	0.02	0.01	0.00	0.00	0.00	0.01	0.01	0.00	0.01	0.01	0.01	0.00	0.00	0.00	0.02
K <sub>2</sub> O	0.00	0.01	0.01	0.01	0.00	0.00	0.00	0.00	0.00	0.00	0.00	0.00	0.00	0.01	0.00	0.00	0.00
Si	1.001	0.995	1.004	1.004	1.002	0.996	1.003	0.995	0.998	0.998	1.001	0.998	0.996	0.998	1.003	0.999	0.998
Ti	0.000	0.001	0.000	0.000	0.001	0.000	0.001	0.002	0.000	0.002	0.003	0.004	0.001	0.000	0.001	0.000	0.000
Al	0.000	0.000	0.000	0.000	0.000	0.001	0.000	0.000	0.001	0.000	0.000	0.000	0.000	0.000	0.000	0.000	0.000
Cr	0.000	0.000	0.000	0.000	0.000	0.000	0.000	0.000	0.000	0.000	0.000	0.000	0.000	0.000	0.000	0.000	0.000
Fe <sup>2+</sup>	0.182	0.185	0.190	0.185	0.173	0.182	0.179	0.185	0.184	0.187	0.185	0.190	0.187	0.186	0.185	0.184	0.187
Mn	0.002	0.003	0.003	0.003	0.003	0.003	0.003	0.003	0.003	0.003	0.003	0.003	0.002	0.003	0.003	0.003	0.003
Ni	0.007	0.007	0.007	0.008	0.007	0.008	0.007	0.007	0.008	0.008	0.007	0.008	0.007	0.007	0.008	0.007	0.007
Mg	1.804	1.813	1.791	1.796	1.808	1.810	1.803	1.813	1.807	1.805	1.800	1.802	1.808	1.807	1.798	1.807	1.806
Ca	0.001	0.001	0.002	0.001	0.001	0.001	0.001	0.001	0.001	0.001	0.001	0.001	0.001	0.001	0.001	0.001	0.001
Na	0.000	0.000	0.001	0.000	0.000	0.000	0.000	0.000	0.000	0.000	0.000	0.000	0.000	0.000	0.000	0.000	0.001
K	0.000	0.000	0.000	0.000	0.000	0.000	0.000	0.000	0.000	0.000	0.000	0.000	0.000	0.000	0.000	0.000	0.000
Mg#	90.8	90.7	90.4	90.7	91.3	90.9	91.0	90.7	90.7	90.6	90.7	90.5	90.6	90.7	90.7	90.6	90.6

Notes: Averages are for all analyses from each sample filtered for CaO > 19.5%. Data are in weight percent (wt%); n = number of analyses; molecular formula was calculated for O = 6.

**Table 3 (continued).**

Hole:	153-920D	Average														
Core, section:	5R-2	2R-2	14R-4	15R-1	16R-3	22R-5	22R-3	18R-2	15R-3	20R-5	15R-3	22R-2	18R-4	15R-5	22R-5	
Interval (cm):	76–82	33–38	76–82	8–15	64–70	11–116	19–23	35–41	36–40	54–60	114–119	69–73	86–93	14–22	3–9	
n:	5	11	18	13	22	13	19	5	9	16	13	17	12	13	14	376
SiO <sub>2</sub>	40.09	41.56	41.17	40.85	41.35	41.22	41.08	41.18	41.27	41.12	40.95	40.76	41.54	40.98	40.29	41.17
TiO <sub>2</sub>	0.00	0.01	0.01	0.01	0.01	0.01	0.01	0.00	0.01	0.01	0.01	0.01	0.02	0.01	0.01	0.01
Al <sub>2</sub> O <sub>3</sub>	0.01	0.01	0.01	0.01	0.01	0.01	0.01	0.01	0.01	0.01	0.02	0.01	0.01	0.02	0.01	0.01
Cr <sub>2</sub> O <sub>3</sub>	0.01	0.00	0.01	0.00	0.02	0.01	0.01	0.02	0.01	0.01	0.02	0.01	0.02	0.01	0.01	0.01
FeO	9.25	9.52	9.09	9.25	9.04	8.96	9.05	9.19	9.22	9.04	9.45	9.03	9.43	9.02	9.17	9.15
MnO	0.13	0.13	0.13	0.13	0.13	0.13	0.13	0.14	0.13	0.13	0.12	0.12	0.15	0.13	0.14	0.13
NiO	0.38	0.37	0.37	0.38	0.38	0.38	0.38	0.39	0.44	0.38	0.38	0.38	0.39	0.40	0.38	0.38
MgO	50.45	50.46	50.25	49.98	50.66	50.14	49.91	50.02	50.04	50.19	49.97	49.80	50.81	50.23	49.26	50.06
CaO	0.04	0.03	0.04	0.04	0.06	0.03	0.06	0.04	0.04	0.02	0.06	0.04	0.04	0.04	0.05	0.04
Na <sub>2</sub> O	0.01	0.01	0.01	0.01	0.02	0.00	0.04	0.01	0.02	0.01	0.01	0.02	0.01	0.01	0.01	0.01
K <sub>2</sub> O	0.01	0.00	0.00	0.01	0.01	0.01	0.01	0.00	0.01	0.00	0.01	0.01	0.01	0.01	0.01	0.01
Si	0.980	0.997	0.996	0.994	0.994	0.998	0.998	0.997	0.998	0.996	0.993	0.995	0.994	0.994	0.993	0.997
Ti	0.000	0.003	0.004	0.002	0.002	0.001	0.005	0.000	0.002	0.004	0.003	0.000	0.002	0.003	0.000	0.053
Al	0.000	0.000	0.000	0.000	0.000	0.000	0.000	0.000	0.001	0.000	0.000	0.000	0.001	0.001	0.000	
Cr	0.000	0.000	0.000	0.000	0.000	0.000	0.000	0.000	0.000	0.000	0.000	0.000	0.000	0.000	0.000	
Fe <sup>2+</sup>	0.189	0.191	0.184	0.188	0.182	0.182	0.184	0.186	0.186	0.183	0.192	0.184	0.189	0.183	0.189	0.185
Mn	0.002	0.003	0.003	0.003	0.003	0.003	0.003	0.003	0.003	0.003	0.003	0.003	0.003	0.003	0.003	0.003
Ni	0.007	0.007	0.007	0.007	0.007	0.007	0.008	0.008	0.008	0.008	0.007	0.007	0.008	0.007	0.008	0.007
Mg	1.839	1.804	1.812	1.812	1.816	1.810	1.807	1.806	1.804	1.812	1.807	1.812	1.812	1.816	1.811	1.808
Ca	0.001	0.001	0.001	0.001	0.002	0.001	0.002	0.001	0.001	0.001	0.002	0.001	0.001	0.001	0.001	0.001
Na	0.000	0.000	0.000	0.000	0.001	0.000	0.000	0.000	0.001	0.000	0.000	0.001	0.000	0.000	0.000	0.000
K	0.000	0.000	0.000	0.000	0.000	0.000	0.000	0.000	0.000	0.000	0.000	0.000	0.000	0.000	0.000	0.000
Mg#	90.7	90.4	90.8	90.6	90.9	90.9	90.8	90.7	90.6	90.8	90.4	90.8	90.6	90.9	90.5	90.7

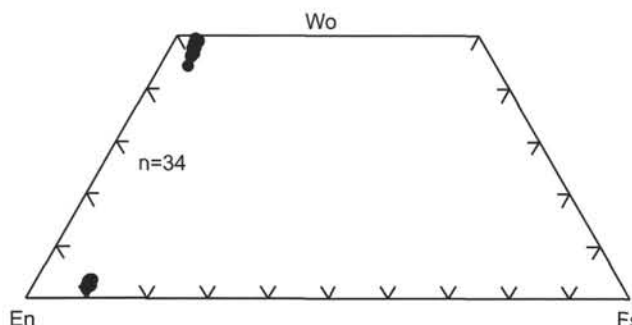


Figure 3. Average clinopyroxene and orthopyroxene microprobe compositions on a per sample basis for Site 920 peridotites. Data are cut for  $\text{CaO} > 19.5\%$  in clinopyroxene and  $\text{CaO} < 3\%$  in orthopyroxene to remove the effects of  $\text{CaO}$  variation caused by exsolution. Wo = wollastonite, En = enstatite, Fs = ferrosilite.

LREE for the elements La–Nd. The group contains rocks that have modal abundances of orthopyroxene ranging from 14.1 to 28.5 modal% orthopyroxene, although all but one have modal orthopyroxene greater than 18%, and modal clinopyroxene ranging up to 3.65%. The extent of REE depletion cannot, therefore, be related directly to the apparent modal mineralogy.

The LREE-depleted pattern can be modeled for residual compositions calculated for 15%–22% fractional melting of fertile spinel peridotite. The steeper LREE pattern evident in the peridotites may be either a function of the sensitivity of the analytical technique at the very low levels of LREE, the choice of distribution coefficients in melting models, or real depletions, but is not easily constrained at this time. It is notable that, in this model, the residual clinopyroxene abundances fell below 3 modal% for 15% melting, and all clinopyroxene is exhausted at about 22% melting.

A second group of Site 920 peridotites (HREE-depleted; Fig. 7B) shows flatter, more-depleted, HREE patterns, with strong depletions in LREE ( $<0.003 \times \text{chondrite}$ ) and moderate-to-strong, positive Eu anomalies. Note that the greatest variation in the smoothness of the profiles is in Eu, which is present in abundances of 1–10 ppb for most samples, and therefore is most susceptible to inaccuracies in the analytical determination. Both of these samples are completely serpentinized granular dunite.

Members of the third group of peridotites have similar HREE patterns to the first group, but are comparatively enriched in La, Ce, and Pr (LREE-enriched-1 group; Fig. 7C), and are transitional in their nature to a group that have even higher LREE abundances.

The last identified group of peridotites displays relatively flat REE patterns, in which REEs between Sm and Yb are indistinguishable from the first three groups (Fig. 8), but La, Ce, Pr, and Nd are relatively enriched to levels of up to  $0.2 \times \text{chondrite}$  ( $\text{La}_N/\text{Yb}_N$  up to 0.25; LREE-enriched-2 group; Fig. 7D).

The comparatively enriched character of the LREE-enriched-2 group of samples is also reflected in the Zr abundances, containing from 71 to 166 ppb Zr, compared with typical ranges of 30–86 for the other groups. Even this correlation is not a strong one, however, because the highest Zr abundances are in samples that occur in the La-enriched-1 group (182 ppb; A5), and in a dunite in the HREE-depleted group (196 ppb; 11).

REE patterns such as observed here (Johnson et al., 1990; Dostal and Muecke, 1977; Pallister and Knight, 1981; Prinzhofer and Allegre, 1985), characterized by V-shaped inflections in the chondrite-normalized patterns in the middle REE, have been modeled in terms of chromatographic metasomatism (Navon and Stolper, 1987; Bodenier et al., 1990; Takazawa et al., 1992). This mechanism of enrichment can account for the selective enrichment of some elements over others based on their relative incompatibility, and may account here for the erratic behavior of the HFSE. Modeling by Navon and Stolper (1987) suggests that low levels of enrichment of REE and inflections

in the chondrite-normalized REE patterns at Nd to Sm are indicative of starved metasomatism, consistent with the absence of any major-element mineral chemical reflection of the process.

Although evidence for rare interstitial magmatic clinopyroxene is present in some samples of Site 920 peridotite (e.g., Shipboard Scientific Party, 1995; Casey, this volume), magmatic clinopyroxene is unlikely to have the sufficiently high  $\text{La}_N/\text{Yb}_N (>10^2)$  required such that small ( $<<1\%$ ) modal abundances could significantly increase the  $\text{LREE}_N$  values, while not effecting the  $\text{HREE}_N$  values. On this basis, the presence of interstitial mineral grains as the site for the enriched components is considered unlikely. Trace-element data on clinopyroxene (Ross and Elthon, Chapter 13, this volume) also show no evidence for significant LREE enrichment, and the physical location of the enriched component thus remains speculative.

## DISCUSSION

In contrast to shipboard observations that there is a significant variation in the modal composition of Site 920 peridotites, mineral chemistry, major-, and trace-element data suggest that these rocks are compositionally homogeneous. The mineral compositions fall consistently within the range predicted from regional variations based on dredge, and limited drill, recoveries. The cause of the apparent modal layering must then reflect grain-size reduction in distinct layers during deformation (Ceuleneer and Cannat, this volume; Fletcher, Ceuleneer, et al., this volume), and subsequent masking of the fine-grained mineralogy by serpentinization.

The depth at which this deformation occurs should be generally, although not exclusively, able to be constrained to relatively shallow depths because of the association of some fine-grained zones with evidence of melt extraction and/or passage, such as veins and dikes of pyroxenite and gabbro (*sensu lato*). Features such as these must intrude at shallow depths to persist as discrete entities to the base of the crust (Ceuleneer and Raboniwicz, 1993). The homogeneous composition of mineral phases in peridotite, including spinel in crosscutting “trails,” however, suggests that the bulk chemistry of the peridotite, except for minor true dunite, reflects homogenization at depths within the mantle corresponding to those close to the solidus. It is thus likely that later veins have utilized existing granular inhomogeneities, and are unrelated to the grain-size reduction process.

There is abundant evidence for subsolidus processes operating that could have affected the chemistry of individual components, or the overall geochemistry, of the system. Low-temperature reequilibration of the mineral chemistry is reflected in the development of exsolution lamellae and “granule exsolution” (Shipboard Scientific Party, 1995). These textures, and evidence for subsolidus element mobility, are particularly evident for clinopyroxene, and range from the presence of exsolution lamellae-free rims on clinopyroxene, to ~0.5 mm blebs within orthopyroxene grains, and to the development of equigranular mosaics of clinopyroxene along subgrain boundaries.

The abundance of plagioclase-bearing dikelets, the occurrence of trails of spinel with low Cr#, apatite, and rarely plagioclase, crosscutting the predominant foliation, and the occurrence of patches containing apatite, zircon, and chlorite within the Site 920 peridotites (Shipboard Scientific Party, 1995) attest to the fact that fluids enriched in incompatible elements have infiltrated the peridotites, perhaps in many cases as through-going melt flow zones, and left pockets of trapped melt.

Trace-element data, nonetheless, contain evidence for the presence of a background matrix of depleted peridotite with compositions little modified since melt extraction (Fig. 7A), and which are distributed evenly throughout the drill holes (Fig. 8). These samples are those with chondrite-normalized REE patterns that can be modeled in terms of 15% to 20% fractional melting of spinel peridotite.

Peridotite with comparatively LREE-enriched bulk compositions is also present. The most enriched samples are localized at a depth of about 100 meters below seafloor in both Holes 920B and 920D (Fig.

**Table 4.** Average clinopyroxene compositions for peridotites from Site 920.

Hole:	153-920B	153-920D														
Core, section:	13R-1	12R-5	12R-4	13R-2	2R-1	1W-3	10R-1	12R-5	13R-2	14R-3	7R-2	12R-1	12R-3	6R-3	12R-3	5R-2
Interval (cm):	66–72	18–23	84–90	114–120	20–26	70–73	102–108	23–28	107–114	7–12	71–78	73–78	29–35	63–68	35–39	76–82
n:	14	10	11	7	1	9	5	12	15	15	11	7	6	16	8	1
SiO <sub>2</sub>	51.84	52.28	51.25	51.52	53.14	51.75	51.94	52.04	51.82	52.21	52.33	52.31	52.26	52.08	50.72	
TiO <sub>2</sub>	0.10	0.09	0.10	0.11	0.10	0.12	0.10	0.10	0.09	0.11	0.12	0.12	0.12	0.13	0.15	
Al <sub>2</sub> O <sub>3</sub>	4.69	4.41	4.87	4.72	3.72	4.84	4.82	4.91	4.43	4.83	4.50	4.73	3.97	4.63	4.60	5.35
Cr <sub>2</sub> O <sub>3</sub>	1.08	0.99	1.18	1.12	1.01	1.21	1.21	1.15	1.01	1.16	1.08	1.26	0.96	1.16	1.17	1.40
FeO	2.44	2.48	2.39	2.45	2.21	2.31	2.65	2.45	2.55	2.73	2.32	2.17	2.22	2.22	2.17	2.25
MnO	0.09	0.08	0.08	0.09	0.13	0.08	0.08	0.09	0.10	0.08	0.09	0.08	0.08	0.08	0.09	0.09
NiO	0.06	0.03	0.05	0.04	0.05	0.06	0.05	0.06	0.05	0.06	0.05	0.05	0.06	0.05	0.07	0.05
MgO	16.71	17.03	15.91	16.49	17.04	16.22	17.21	16.48	16.97	16.94	16.75	16.43	16.59	16.63	16.51	15.97
CaO	23.14	22.89	23.36	22.80	23.96	23.51	22.34	23.26	22.59	22.47	23.33	23.53	23.51	23.41	23.41	23.27
Na <sub>2</sub> O	0.06	0.07	0.06	0.09	0.04	0.07	0.08	0.07	0.07	0.10	0.07	0.13	0.10	0.09	0.10	0.03
K <sub>2</sub> O	0.00	0.01	0.01	0.00	0.00	0.00	0.01	0.00	0.00	0.00	0.01	0.00	0.00	0.00	0.00	0.00
Si	1.881	1.892	1.880	1.884	1.906	1.880	1.877	1.881	1.888	1.878	1.888	1.886	1.903	1.887	1.887	1.861
Ti	0.003	0.003	0.003	0.003	0.003	0.003	0.003	0.003	0.002	0.003	0.003	0.004	0.003	0.003	0.003	0.004
Al	0.200	0.188	0.210	0.203	0.157	0.207	0.205	0.209	0.190	0.206	0.192	0.201	0.170	0.197	0.197	0.231
Cr	0.031	0.028	0.034	0.033	0.030	0.037	0.034	0.033	0.030	0.033	0.031	0.037	0.030	0.034	0.031	0.040
Fe <sup>2+</sup>	0.074	0.075	0.073	0.075	0.066	0.070	0.080	0.074	0.078	0.083	0.070	0.066	0.068	0.067	0.066	0.069
Mn	0.003	0.002	0.003	0.002	0.004	0.002	0.003	0.003	0.003	0.003	0.003	0.002	0.003	0.003	0.003	0.003
Ni	0.002	0.001	0.001	0.001	0.001	0.002	0.002	0.002	0.001	0.002	0.001	0.001	0.002	0.002	0.002	0.001
Mg	0.904	0.919	0.870	0.898	0.911	0.878	0.927	0.888	0.921	0.915	0.903	0.883	0.900	0.895	0.892	0.873
Ca	0.900	0.887	0.918	0.893	0.921	0.915	0.866	0.901	0.882	0.873	0.904	0.909	0.916	0.906	0.909	0.915
Na	0.004	0.005	0.005	0.006	0.003	0.005	0.006	0.005	0.005	0.007	0.005	0.009	0.007	0.006	0.007	0.002
K	0.000	0.000	0.000	0.000	0.000	0.000	0.000	0.000	0.000	0.000	0.000	0.000	0.000	0.000	0.000	0.000
Mg#	92.45	92.43	92.23	92.31	93.24	92.61	92.06	92.31	92.22	91.70	92.77	93.09	93.02	93.04	93.15	92.68
Cr#	13.56	12.97	13.78	13.92	16.04	15.05	14.23	13.45	13.62	13.69	13.89	15.62	15.00	14.64	13.72	14.76
Wo	47.93	47.17	49.33	47.85	48.52	49.10	46.22	48.36	46.89	46.66	48.16	48.93	48.64	48.50	48.68	49.27
En	48.14	48.83	46.73	48.14	48.00	47.14	49.51	47.67	48.98	48.91	48.09	47.53	47.77	47.91	47.80	47.01
Fs	3.93	4.00	3.94	4.01	3.48	3.76	4.27	3.97	4.13	4.43	3.75	3.53	3.58	3.58	3.52	3.72

Notes: Averages are for all analyses from each sample filtered for CaO > 19.5%. Data are in weight percent (wt%); n = number of analyses; molecular formula was calculated for O = 6. Wo = wollastonite content, En = enstatite content, Fs = ferrosilite content.

**Table 4 (continued).**

Hole:	153-920D	Average														
Core, section:	5R-2	2R-2	14R-4	15R-1	16R-3	22R-5	22R-3	18R-2	15R-3	20R-5	15R-3	22R-2	18R-4	15R-5	22R-5	
Interval (cm):	76–82	33–38	76–82	8–15	64–70	11–116	19–23	35–41	36–40	54–60	114–119	69–73	86–93	14–22	3–9	
n:	1	2	16	13	27	18	9	12	12	27	17	14	3	17	21	365
SiO <sub>2</sub>	50.72	52.17	52.01	51.67	51.87	51.74	51.85	51.40	51.95	51.71	51.86	50.74	51.59	51.85	50.92	51.77
TiO <sub>2</sub>	0.15	0.13	0.10	0.09	0.10	0.12	0.11	0.17	0.10	0.10	0.12	0.12	0.12	0.11	0.11	0.11
Al <sub>2</sub> O <sub>3</sub>	5.35	4.90	4.77	4.69	4.89	4.59	4.67	5.24	4.93	4.47	4.69	5.25	5.02	4.50	4.89	4.72
Cr <sub>2</sub> O <sub>3</sub>	1.40	1.29	1.08	1.13	1.16	1.11	1.06	1.28	1.15	1.02	1.11	1.28	1.28	0.99	1.19	1.12
FeO	2.25	2.12	2.65	2.75	2.73	2.59	2.64	2.38	2.84	2.33	2.78	2.56	2.39	2.59	2.58	2.52
MnO	0.09	0.10	0.09	0.10	0.10	0.10	0.07	0.09	0.07	0.07	0.10	0.10	0.08	0.09	0.08	0.09
NiO	0.05	0.05	0.06	0.04	0.04	0.06	0.04	0.06	0.06	0.05	0.05	0.06	0.05	0.04	0.05	0.05
MgO	15.97	16.30	17.05	17.02	17.34	16.64	16.94	16.06	17.58	16.78	17.05	16.28	16.54	17.15	16.21	16.75
CaO	23.27	23.85	22.66	22.48	22.31	22.72	22.25	23.59	21.31	23.08	22.45	22.67	23.72	22.46	23.50	22.87
Na <sub>2</sub> O	0.03	0.10	0.07	0.08	0.10	0.08	0.11	0.11	0.08	0.08	0.11	0.11	0.21	0.08	0.11	0.09
K <sub>2</sub> O	0.00	0.02	0.00	0.01	0.01	0.01	0.01	0.01	0.01	0.00	0.01	0.01	0.00	0.00	0.01	0.01
Si	1.861	1.879	1.880	1.878	1.873	1.886	1.887	1.866	1.881	1.886	1.880	1.863	1.863	1.886	1.865	1.880
Ti	0.004	0.004	0.003	0.002	0.003	0.003	0.003	0.005	0.003	0.003	0.003	0.003	0.003	0.003	0.003	0.003
Al	0.231	0.208	0.203	0.201	0.208	0.197	0.200	0.224	0.210	0.192	0.200	0.227	0.213	0.193	0.211	0.202
Cr	0.040	0.040	0.031	0.032	0.032	0.030	0.036	0.032	0.031	0.030	0.038	0.037	0.029	0.035	0.032	
Fe <sup>2+</sup>	0.069	0.064	0.080	0.084	0.082	0.079	0.080	0.072	0.086	0.071	0.084	0.079	0.072	0.079	0.079	0.077
Mn	0.003	0.003	0.003	0.003	0.003	0.003	0.003	0.002	0.003	0.002	0.003	0.003	0.002	0.003	0.002	0.003
Ni	0.001	0.002	0.002	0.001	0.001	0.002	0.001	0.002	0.002	0.001	0.001	0.002	0.001	0.001	0.002	0.001
Mg	0.873	0.875	0.919	0.922	0.933	0.904	0.918	0.869	0.948	0.912	0.921	0.891	0.890	0.930	0.885	0.907
Ca	0.915	0.920	0.878	0.876	0.863	0.887	0.868	0.918	0.827	0.902	0.872	0.892	0.918	0.875	0.923	0.890
Na	0.002	0.007	0.005	0.006	0.007	0.006	0.008	0.007	0.006	0.006	0.008	0.008	0.015	0.006	0.008	0.006
K	0.000	0.001	0.000	0.000	0.000	0.000	0.000	0.000	0.000	0.000	0.000	0.000	0.000	0.000	0.000	0.000
Mg#	92.68	93.18	91.98	91.69	91.89	91.98	91.96	92.33	91.69	92.76	91.63	91.90	92.52	92.18	91.81	92.22
Cr#	14.76	16.13	13.11	13.87	13.41	14.06	13.04	13.79	13.11	13.81	13.03	14.30	14.67	13.24	14.31	13.80
Wo	49.27	49.49	46.77	46.54	45.95	47.43	46.49	49.36	44.42	47.84	46.45	47.91	48.82	46.47	48.90	47.51
En	47.01	47.07	48.96	49.01	49.67	48.35	49.21	46.76	50.96	48.38	49.07	47.86	47.35	49.35	46.91	48.40
Fs	3.72	3.44	4.27	4.44	4.38	4.22	4.30	3.88	4.62	3.77	4.48	4.22	3.83	4.19	4.19	4.08

8), at the level where granular dunite zones were recovered. Whole-rock chemical data suggest that these are cumulate dunites for which the bulk rock Mg# is slightly less (about 90) than that measured for Mg# of olivine in peridotite (average 90.7). These data suggest that the dunites are residual after the localized passage of a melt that crystallized olivine in the manner suggested by Takazawa et al. (1992).

Onboard discussion (Shipboard Scientific Party, 1995) noted the occurrence of black, sheared, pyroxene-poor harzburgite to dunite in the vicinity of gabbro and pyroxenite (*sensu lato*) veins (see, for example, Casey, this volume; Niida, this volume), and centered around whether the dunites and highly depleted harzburgites were residual after the removal of pyroxene by melting in close association with the observed veins, or early-formed olivine-rich zones that had localized deformation and fluid migration resulting from their relative ductility under shear stress.

Impregnation marginal to individual veinlets, however, is shown to be restricted to enrichments in mineral chemistry on a centimeter scale (Niida, this volume). Samples investigated in this study were selected in intervals of good core recovery, however, such that the likelihood of nearby veins, which were not recovered by drilling, contributing to the enrichment was minimized. The homogeneous mineral chemistry of peridotite phases argues against melt being sweated from, or interacting with, the adjacent wall rocks on a broad scale. Melt passage that left its signature in the presence of the granular dunite zone was most probably related to a broader metasomatic event that has left a more pervasive signature on the surrounding peridotite.

## ACKNOWLEDGMENTS

Access to analytical facilities and funding for analyses was supported partly by Professor K.D. Collerson, Head, The Department of Earth Sciences, The University of Queensland. Y. Niu assisted with ICP-MS analyses and freely discussed the concept of excess olivine. These discussions significantly advanced this paper, as did reviews by R. Hebert and D. Elthon.

## REFERENCES

- Bodinier, J.L., Vasseur, G., Vernieres, J., Dupuy, C., and Fabries, J., 1990. Mechanisms of mantle metasomatism: geochemical evidence from the Lherz Orogenic Peridotite. *J. Petrol.*, 31:597–628.
- Cannat, M., Bideau, D., and Hebert, R., 1990. Plastic deformation and magmatic impregnation in serpentinized ultramafic rocks from the Garrett transform fault (East Pacific Rise). *Earth Planet. Sci. Lett.*, 101:216–232.
- Cannat, M., and Casey, J.F., 1995. An ultramafic lift at the Mid-Atlantic Ridge: successive stages of magmatism in serpentinized peridotites from the 15°N region. In Vissers, R.L.M., and Nicolas, A. (Eds.), *Mantle and Lower Crust Exposed in Oceanic Ridges and Ophiolites*: Dordrecht (Kluwer), 5–34.
- Ceuleneer, G., and Rabinowicz, M. 1993. Mantle flow and melt migration beneath oceanic ridges: models derived from observations in ophiolites. In Phipps Morgan, J., Blackman, D.K. and Sinton, J.M. (Eds.) *Mantle Flow and Melt Generation at Mid-Ocean Ridges*. Am. Geophys. Union, Geophysical Monograph 71: 123–154.
- Dick, H.J.B., 1989. Abyssal peridotites, very slow spreading ridges and ocean ridge magmatism. In Saunders, A.D., and Norry, M.J. (Eds.), *Magmatism in the Ocean Basins*. Geol. Soc. Spec. Publ. London, 42:71–105.
- Dick, H.J.B., Fisher, R.L., and Bryan, W.B., 1984. Mineralogic variability of the uppermost mantle along mid-ocean ridges. *Earth Planet. Sci. Lett.*, 69:88–106.
- Dostal, J., and Muecke, G.K., 1977. Trace element geochemistry of igneous rocks from Site 334, Leg 37. In Aumento, F., and Nelson, W.G., et al., *Init. Repts. DSDP*, 37: Washington (U.S. Govt. Printing Office), 573–576.
- Elthon, D., 1992. Chemical trends in abyssal peridotites: refertilization of depleted suboceanic mantle. *J. Geophys. Res.*, 97:9015–9025.
- Ewart, A., and Hawkesworth, C.J., 1987. The Pleistocene-Recent Tonga-Kermadec arc lavas: interpretation of new isotope and rare earth data in terms of a depleted mantle source model. *J. Petrol.*, 28:495–530.
- Forsyth, D.W., 1993. Geophysical constraints on mantle flow and melt generation beneath mid-ocean ridges. In Phipps Morgan, J., Blackman, D.K., and Sinton, J.M. (Eds.), *Mantle Flow and Melt Generation at Mid-Ocean Ridges*. Geophys. Monogr., Am. Geophys. Union, 71:1–66.
- Gruau, G., Bernard-Griffiths, J., Lecuyer, C., Henin, O., Mace, J., and Cannat, M., 1995. Extreme Nd isotopic variation in the Trinity Ophiolite Complex and the role of melt/rock reactions in the oceanic lithosphere. *Contrib. Mineral. Petrol.*, 121:337–350.
- Gruau, G., Lecuyer, C., Bernard-Griffiths, J., and Morin, J., 1991. Origin and petrogenesis of the Trinity Ophiolite Complex (California): new constraints from REE and Nd isotope data. In Menzies, M.A., Dupuy, C., and Nicholas, A. (Eds.), *Orogenic Lherzolites and Mantle Processes*. J. Petrol. Spec. Issue, 229–242.
- Hekinian, R., Thompson, G., and Bideau, D., 1989. Axial and off-axis heterogeneity of basaltic rocks from the East Pacific Rise at 12°35'N–12°51'N and 11°26'N–11°30'N. *J. Geophys. Res.*, 94:17437–17463.
- Hess, P.C., 1993. Phase equilibria constraints on the origin of ocean floor basalts. In Phipps Morgan, J., Blackman, D.K., and Sinton, J.M. (Eds.), *Mantle Flow and Melt Generation at Mid-Ocean Ridges*. Geophys. Monogr., Am. Geophys. Union, 71:67–102.
- Jacobsen, S.B., Quick, J.E., and Wasserburg, G.J., 1984. A Nd and Sr isotopic study of the Trinity peridotite: implications for mantle evolution. *Earth Planet. Sci. Lett.*, 50:139–155.
- Jacques, A.L., and Green, D.H., 1980. Anhydrous melting of peridotite at 0–15 kb pressure and the genesis of tholeiitic basalts. *Contrib. Mineral. Petrol.*, 73:287–310.
- Jagoutz, E., Palme, H., Baddenhausen, H., Blum, K., Cendales, M., Dreibus, G., Spettel, B., Lorenz, V., and Waenke, H., 1979. The abundances of major, minor and trace elements in the Earth's mantle as derived from primitive ultramafic nodules. *Proc. 10th Lunar Planet. Sci. Conf.*, 2031–2050.
- Johnson, K.T.M., Dick, H.J.B., and Shimizu, N., 1990. Melting in the oceanic upper mantle: an ion microprobe study of diopside in abyssal peridotites. *J. Geophys. Res.*, 95:2661–2678.
- Juteau, T., Berger, E., and Cannat, M., 1990. Serpentized, residual mantle peridotites from the M.A.R. median valley, ODP Hole 670A (21°10'N, 45°02'W, Leg 109): primary mineralogy and geothermometry. In Detrick, R., Honnorez, J., Bryan, W.B., Juteau, T., et al., *Proc. ODP, Sci. Results*, 106/109: College Station, TX (Ocean Drilling Program), 27–45.
- Klein, E.M., and Langmuir, C.H., 1987. Global correlations of ocean ridge basalts chemistry with axial depth and crustal thickness. *J. Geophys. Res.*, 92:8089–8115.
- Langmuir, C.H., Klein, E.M., and Plank, T. 1993. Petrological systematics of mid-ocean ridge basalts: Constraints on melt generation beneath mid-ocean ridges. In Phipps Morgan, J., Blackman, D.K., and Sinton, J.M. (Eds.), *Mantle Flow and Melt Generation at Mid-Ocean Ridges*. Am. Geophys. Union, Geophysical Monograph 71: 183–280.
- McKenzie, D., and Bickle, M.J., 1988. The volume and composition of melt generated by extension of the lithosphere. *J. Petrol.*, 29:625–679.
- Michael, P.J., and Bonatti, E., 1985. Peridotite composition from the North Atlantic: regional and tectonic variations and implications for partial melting. *Earth Planet. Sci. Lett.*, 73:91–104.
- Mysen, B.O., and Kushiro, I., 1977. Compositional variations of coexisting phases with degree of melting of peridotite in the upper mantle. *Am. Mineral.*, 62:843–865.
- Navon, O., and Stolper, E., 1987. Geochemical consequences of melt percolation: the upper mantle as a chromatographic column. *J. Geol.*, 95:285–307.
- Niu, Y., and Batiza, R., 1993. Melting processes under fast and slow mid-ocean ridges. IAVCEI General Assembly, September 1993, Canberra, Australia, 8. (Abstract)
- Niu, Y., Langmuir, C.H., and Kinzler, R.J., 1995. Oceanic peridotite genesis and mantle melting beneath slow-spreading ridges. *Terra Nova*, 7:144.
- Pallister, J.S., and Knight, R.J., 1981. Rare-earth element geochemistry of the Samail ophiolite near Ibra, Oman. *J. Geophys. Res.*, 86:2673–2697.
- Parsons, B., and Slater, J.G., 1977. An analysis of the variation of ocean floor bathymetry and heat flow with age. *J. Geophys. Res.*, 82:803–827.
- Prinzhofer, A., and Allègre, C.J., 1985. Residual peridotites and the mechanisms of partial melting. *Earth Planet. Sci. Lett.*, 74:251–265.

- Quick, J.E., 1981. Petrology and petrogenesis of the Trinity Peridotite, an upper mantle diapir in the eastern Klamath Mountains, northern California. *J. Geophys. Res.*, 86:11837–11863.
- Ross, K., and Elthon, D., 1993. Cumulates from strongly depleted mid-ocean-ridge basalt. *Nature*, 365:826–829.
- Shibata, T., and Thompson, G., 1986. Peridotites from the Mid-Atlantic Ridge at 43°N and their petrogenetic relation to abyssal tholeiites. *Contrib. Mineral. Petrol.*, 93:144–159.
- Shipboard Scientific Party, 1995. Site 920. In Cannat, M., Karson, J.A., Miller, D.J., et al., *Proc. ODP, Init. Repts.*, 153: College Station, TX (Ocean Drilling Program), 45–119.
- Sun, S.-S., and McDonough, W.F., 1989. Chemical and isotopic systematics of oceanic basalts: implications for mantle compositions and processes. *In* Saunders, A.D., and Norry, M.J. (Eds.), *Magmatism in the Ocean Basins*. Geol. Soc. Spec. Publ. London, 42:313–345.
- Takahashi, N., 1992. Evidence for melt segregation toward fractures in the Horoman mantle peridotite complex. *Nature*, 359:52–55.
- Takazawa, E., Frey, F.A., Shimizu, N., Obata, M., and Bodinier, J.L., 1992. Geochemical evidence for melt migration and reaction in the upper mantle. *Nature*, 359:55–58.

Date of initial receipt: 21 August 1995

Date of acceptance: 1 May 1996

Ms 153SR-016

**Table 5. Average orthopyroxene compositions for peridotites from Site 920.**

Hole:	153-920B	153-920D	153-920D	153-920D	153-920D	153-920D	153-920D										
Core, section:	13R-1	12R-5	12R-4	13R-2	2R-1	3R-2	4R-1	1W-3	10R-1	12R-5	13R-2	14R-3	7R-2	12R-1	12R-3	6R-3	12R-3
Interval (cm):	66–72	18–23	84–90	114–120	20–26	82–89	129–136	70–73	102–108	23–28	107–114	7–12	71–78	73–78	29–35	63–68	35–39
n:	3	4	2	8	4	6	7	8	6	5	4	15	9	7	4	8	6
SiO <sub>2</sub>	54.69	55.14	54.40	55.14	55.65	54.62	55.58	55.45	55.36	54.96	55.27	55.44	55.34	55.75	55.08	55.45	55.65
TiO <sub>2</sub>	0.04	0.03	0.06	0.05	0.03	0.03	0.05	0.03	0.05	0.04	0.02	0.05	0.04	0.03	0.04	0.03	0.06
Al <sub>2</sub> O <sub>3</sub>	4.63	4.19	4.78	3.91	4.37	4.23	4.18	3.79	4.27	4.74	3.83	3.87	3.85	4.13	4.01	4.20	3.94
Cr <sub>2</sub> O <sub>3</sub>	0.99	0.81	1.03	0.77	0.87	0.83	0.85	0.71	0.91	0.94	0.73	0.72	0.77	0.86	0.81	0.88	0.78
FeO	5.71	5.95	5.82	5.91	5.96	5.98	5.91	5.92	5.91	5.97	5.95	6.12	6.06	6.03	5.87	6.00	5.96
MnO	0.12	0.15	0.14	0.14	0.13	0.13	0.14	0.14	0.13	0.14	0.15	0.15	0.13	0.13	0.14	0.14	0.13
NiO	0.08	0.10	0.10	0.09	0.08	0.11	0.12	0.09	0.12	0.11	0.10	0.08	0.10	0.10	0.11	0.10	0.10
MgO	32.48	32.69	31.48	32.17	33.03	32.83	32.98	33.00	32.52	32.52	32.53	32.71	33.13	32.98	32.21	32.67	33.04
CaO	1.74	1.23	1.86	1.32	1.01	1.55	1.18	1.50	1.63	1.41	1.15	1.42	1.18	1.22	1.76	1.56	1.22
Na <sub>2</sub> O	0.01	0.01	0.00	0.00	0.01	0.01	0.02	0.01	0.02	0.01	0.01	0.01	0.01	0.01	0.01	0.01	0.00
K <sub>2</sub> O	0.01	0.01	0.00	0.00	0.01	0.01	0.01	0.01	0.00	0.01	0.01	0.01	0.01	0.01	0.01	0.01	0.01
Si	1.885	1.902	1.892	1.916	1.902	1.888	1.903	1.907	1.900	1.888	1.915	1.909	1.904	1.905	1.907	1.901	1.908
Ti	0.001	0.001	0.002	0.001	0.001	0.001	0.001	0.002	0.001	0.001	0.001	0.001	0.001	0.001	0.001	0.001	0.002
Al	0.188	0.170	0.196	0.160	0.176	0.172	0.169	0.154	0.173	0.192	0.157	0.157	0.156	0.166	0.163	0.170	0.159
Cr	0.030	0.020	0.030	0.020	0.023	0.022	0.023	0.020	0.025	0.024	0.020	0.021	0.020	0.023	0.020	0.021	0.020
Fe <sup>2+</sup>	0.165	0.172	0.169	0.172	0.171	0.173	0.169	0.170	0.170	0.172	0.173	0.176	0.174	0.172	0.170	0.172	0.171
Mn	0.004	0.004	0.004	0.004	0.004	0.004	0.004	0.004	0.004	0.004	0.004	0.004	0.004	0.003	0.004	0.004	0.004
Ni	0.002	0.003	0.003	0.002	0.002	0.003	0.003	0.003	0.003	0.003	0.002	0.003	0.003	0.003	0.003	0.003	0.003
Mg	1.669	1.681	1.633	1.666	1.683	1.692	1.683	1.692	1.664	1.665	1.681	1.679	1.699	1.680	1.662	1.670	1.689
Ca	0.064	0.045	0.069	0.049	0.037	0.057	0.043	0.056	0.060	0.052	0.043	0.052	0.043	0.045	0.065	0.057	0.045
Na	0.000	0.001	0.000	0.000	0.001	0.001	0.002	0.001	0.001	0.001	0.001	0.001	0.001	0.001	0.001	0.001	0.000
K	0.000	0.000	0.000	0.000	0.000	0.000	0.000	0.000	0.000	0.000	0.000	0.000	0.000	0.000	0.000	0.000	0.000
Mg#	91.02	90.73	90.62	90.65	90.80	90.74	90.87	90.85	90.75	90.66	90.69	90.51	90.69	90.69	90.72	90.66	90.81
Cr#	13.74	10.51	13.30	11.12	11.35	11.17	11.93	11.53	12.64	11.11	11.33	11.63	11.36	12.08	10.91	11.14	11.17
Wo	3.39	2.38	3.69	2.60	1.93	2.98	2.28	2.89	3.19	2.75	2.24	2.74	2.27	2.37	3.43	3.02	2.36
En	87.94	88.57	87.28	88.29	89.04	88.03	88.80	88.22	87.86	88.16	88.66	88.03	88.63	88.54	87.61	87.92	88.67
Fs	8.67	9.05	9.04	9.11	9.02	8.98	8.92	8.88	8.96	9.09	9.10	9.23	9.10	9.09	8.96	9.06	8.97

Notes: Averages for all analyses for each sample filtered for CaO < 3%. Data are in weight percent (wt%); molecular formula was calculated for O = 6. Other abbreviations as in Table 4.

**Table 5 (continued).**

Hole:	153-920D	Average														
Core, section:	5R-2	2R-2	14R-4	15R-1	16R-3	22R-5	22R-3	18R-2	15R-3	20R-5	15R-3	22R-2	18R-4	15R-5	22R-5	
Interval (cm):	76–82	33–38	76–82	8–15	64–70	11–116	19–23	35–41	36–40	54–60	114–119	69–73	86–93	14–22	3–9	
n:	7	4	17	19	17	9	10	14	4	14	13	12	2	17	8	
															282	
SiO <sub>2</sub>	54.86	55.78	55.30	54.92	55.39	55.20	54.86	54.63	55.07	54.63	55.19	54.94	55.34	55.13	54.19	55.13
TiO <sub>2</sub>	0.03	0.04	0.04	0.05	0.04	0.03	0.04	0.06	0.03	0.04	0.06	0.04	0.04	0.05	0.03	0.04
Al <sub>2</sub> O <sub>3</sub>	4.33	3.98	4.08	4.29	4.14	4.08	3.96	4.96	4.45	4.09	3.76	3.87	4.27	3.88	4.09	4.11
Cr <sub>2</sub> O <sub>3</sub>	0.88	0.84	0.79	0.92	0.84	0.81	0.78	1.02	0.93	0.79	0.73	0.76	0.88	0.71	0.79	0.82
FeO	6.05	6.04	5.94	6.04	5.96	5.94	5.80	6.02	6.35	5.82	6.10	5.83	6.18	5.88	6.03	5.96
MnO	0.14	0.13	0.14	0.13	0.14	0.14	0.13	0.13	0.14	0.14	0.15	0.13	0.11	0.14	0.15	0.14
NiO	0.11	0.08	0.11	0.12	0.11	0.10	0.11	0.10	0.09	0.09	0.11	0.09	0.11	0.09	0.10	0.10
MgO	32.78	33.06	32.98	32.04	33.07	32.58	32.35	32.19	32.47	32.55	32.65	32.44	33.46	32.77	32.37	32.64
CaO	1.35	1.28	1.44	1.77	1.48	1.43	1.76	1.51	1.24	1.62	1.71	1.52	1.08	1.62	1.37	1.48
Na <sub>2</sub> O	0.01	0.01	0.02	0.02	0.01	0.03	0.01	0.01	0.01	0.01	0.02	0.02	0.01	0.02	0.02	0.01
K <sub>2</sub> O	0.01	0.00	0.01	0.01	0.01	0.01	0.02	0.00	0.00	0.00	0.01	0.01	0.00	0.01	0.01	0.01
Si	1.891	1.907	1.899	1.899	1.896	1.904	1.904	1.882	1.895	1.897	1.905	1.908	1.890	1.904	1.895	1.901
Ti	0.001	0.001	0.001	0.001	0.001	0.001	0.001	0.002	0.001	0.001	0.002	0.001	0.001	0.001	0.001	0.001
Al	0.176	0.160	0.165	0.175	0.167	0.166	0.162	0.201	0.180	0.167	0.153	0.158	0.172	0.158	0.169	0.167
Cr	0.024	0.020	0.020	0.025	0.022	0.021	0.020	0.029	0.023	0.020	0.020	0.021	0.020	0.020	0.023	0.022
Fe <sup>2+</sup>	0.175	0.172	0.170	0.175	0.171	0.171	0.168	0.173	0.183	0.169	0.176	0.169	0.177	0.170	0.176	0.172
Mn	0.004	0.004	0.004	0.004	0.004	0.004	0.004	0.004	0.004	0.004	0.004	0.004	0.003	0.004	0.005	0.004
Ni	0.003	0.002	0.003	0.003	0.003	0.003	0.003	0.003	0.003	0.003	0.003	0.003	0.003	0.002	0.003	0.003
Mg	1.684	1.685	1.688	1.652	1.688	1.675	1.674	1.653	1.665	1.685	1.680	1.680	1.703	1.687	1.688	1.678
Ca	0.050	0.047	0.053	0.066	0.054	0.053	0.065	0.056	0.046	0.060	0.063	0.057	0.040	0.060	0.051	0.055
Na	0.001	0.001	0.002	0.001	0.001	0.000	0.002	0.001	0.000	0.001	0.001	0.002	0.001	0.001	0.001	0.001
K	0.000	0.000	0.000	0.000	0.000	0.000	0.001	0.000	0.000	0.000	0.000	0.000	0.000	0.001	0.000	0.000
Mg#	90.61	90.72	90.83	90.44	90.81	90.72	90.86	90.51	90.11	90.89	90.52	90.84	90.61	90.86	90.54	90.70
Cr#	12.13	11.10	10.81	12.62	11.53	11.28	10.99	12.71	11.10	10.69	11.56	11.62	10.42	11.23	11.78	11.59
Wo	2.61	2.47	2.77	3.48	2.83	2.79	3.43	2.96	2.40	3.15	3.29	2.97	2.06	3.12	2.68	2.88
En	88.24	88.48	88.31	87.29	88.24	88.19	87.74	87.83	87.95	88.03	87.54	88.14	88.74	88.03	88.12	88.09
Fs	9.15	9.05	8.92	9.23	8.93	9.02	8.83	9.21	9.65	8.82	9.17	8.89	9.20	8.86	9.20	9.03

**Table 6.** Average chrome spinel compositions for peridotites from Site 920.

Hole:	153-920B	153-920D	153-920D	153-920D	153-920D	153-920D										
Core, section:	13R-1	12R-5	12R-4	13R-2	2R-1	3R-2	4R-1	1W-3	10R-1	12R-5	13R-2	14R-3	7R-2	12R-1	12R-3	6R-3
Interval (cm):	66–72	18–23	84–90	114–120	20–26	82–89	129–136	70–73	102–108	23–28	107–114	7–12	71–78	73–78	29–35	63–68
n:	7	10	3	7	3	5	5	9	9	9	11	14	7	13	8	5
SiO <sub>2</sub>	0.01	0.02	0.01	0.02	0.63	0.05	0.04	0.05	0.04	0.01	0.02	0.06	0.21	0.01	0.02	0.01
TiO <sub>2</sub>	0.05	0.04	0.03	0.05	0.03	0.07	0.07	0.03	0.04	0.03	0.05	0.03	0.04	0.05	0.06	0.04
Al <sub>2</sub> O <sub>3</sub>	45.13	44.29	43.99	44.18	45.16	42.57	42.78	45.36	42.90	42.84	43.47	43.54	44.27	42.73	43.86	48.25
Cr <sub>2</sub> O <sub>3</sub>	24.43	25.12	24.25	24.60	21.99	25.57	25.41	22.91	25.07	24.80	25.47	24.93	23.54	26.23	25.37	20.57
FeO	13.41	13.42	13.93	13.42	13.83	13.05	12.77	13.20	13.78	13.72	13.40	14.31	13.58	13.91	13.32	12.63
MnO	0.17	0.16	0.17	0.16	0.15	0.18	0.17	0.14	0.18	0.18	0.17	0.16	0.14	0.16	0.18	0.14
NiO	0.21	0.20	0.19	0.22	0.17	0.20	0.19	0.23	0.22	0.18	0.22	0.19	0.20	0.19	0.21	0.21
MgO	17.55	17.50	15.83	16.42	17.65	17.37	17.38	17.80	17.54	17.34	16.32	16.99	17.22	17.15	16.27	17.94
CaO	0.01	0.01	0.01	0.00	0.00	0.02	0.00	0.01	0.01	0.01	0.00	0.01	0.01	0.01	0.01	0.06
Na <sub>2</sub> O	0.00	0.00	0.00	0.00	0.00	0.00	0.03	0.00	0.00	0.00	0.01	0.00	0.00	0.01	0.00	0.00
K <sub>2</sub> O	0.00	0.00	0.01	0.00	0.00	0.00	0.01	0.00	0.00	0.01	0.00	0.00	0.01	0.00	0.00	0.01
Si	0.000	0.001	0.001	0.001	0.018	0.000	0.001	0.001	0.000	0.000	0.001	0.002	0.007	0.000	0.001	0.000
Ti	0.001	0.001	0.001	0.001	0.001	0.002	0.001	0.001	0.001	0.001	0.001	0.001	0.001	0.001	0.001	0.001
Al	1.451	1.431	1.464	1.443	1.463	1.412	1.412	1.469	1.406	1.414	1.427	1.421	1.450	1.395	1.441	1.541
Cr	0.526	0.545	0.535	0.548	0.477	0.560	0.560	0.498	0.550	0.549	0.566	0.546	0.513	0.575	0.560	0.442
Fe <sup>2+</sup>	0.306	0.308	0.330	0.311	0.318	0.298	0.301	0.304	0.321	0.320	0.313	0.332	0.311	0.323	0.311	0.287
Mn	0.004	0.004	0.005	0.004	0.004	0.004	0.004	0.003	0.004	0.004	0.004	0.004	0.003	0.004	0.004	0.003
Ni	0.005	0.005	0.005	0.005	0.004	0.005	0.005	0.005	0.005	0.004	0.005	0.004	0.005	0.004	0.004	0.004
Mg	0.714	0.716	0.662	0.685	0.724	0.729	0.725	0.730	0.728	0.724	0.681	0.702	0.716	0.709	0.676	0.725
Ca	0.000	0.000	0.000	0.000	0.000	0.000	0.000	0.000	0.000	0.000	0.000	0.001	0.000	0.000	0.000	0.002
Na	0.000	0.000	0.001	0.000	0.000	0.000	0.000	0.000	0.000	0.000	0.000	0.000	0.000	0.000	0.000	0.000
K	0.000	0.000	0.000	0.000	0.000	0.000	0.000	0.000	0.000	0.000	0.000	0.000	0.000	0.000	0.000	0.000
Mg#	69.99	69.92	66.77	68.76	69.48	71.01	70.65	70.60	69.42	69.33	68.49	67.90	69.73	68.72	68.51	71.67
Cr/(Cr+Al)	26.60	27.59	26.76	27.53	24.58	28.39	28.40	25.31	28.12	27.96	28.39	27.74	26.14	29.17	27.99	22.29

Notes: All data are in weight percent (wt%); molecular formula was calculated for O = 4; n = number of analyses.

**Table 6 (continued).**

Hole:	153-920D	Average														
Core, section:	12R-3	5R-2	2R-2	14R-4	15R-1	16R-3	22R-5	22R-3	18R-2	15R-3	20R-5	15R-3	22R-2	15R-5	22R-5	
Interval (cm):	35–39	76–82	33–38	76–82	8–15	64–70	11–116	19–23	35–41	36–40	54–60	114–119	69–73	14–22	3–9	
n:	10	13	11	15	21	21	17	13	4	12	9	7	15	23	14	336
SiO <sub>2</sub>	0.02	0.04	0.01	0.01	0.03	0.02	0.02	0.02	0.03	0.00	0.36	0.01	0.01	0.02	0.04	
TiO <sub>2</sub>	0.05	0.06	0.06	0.03	0.04	0.05	0.06	0.05	0.05	0.03	0.04	0.05	0.05	0.04	0.05	
Al <sub>2</sub> O <sub>3</sub>	43.59	43.57	42.34	44.02	42.51	43.25	42.06	42.59	43.19	41.66	45.64	41.67	42.57	43.56	43.72	43.35
Cr <sub>2</sub> O <sub>3</sub>	24.68	25.42	26.40	24.54	25.52	25.38	24.89	25.11	25.23	25.85	22.81	24.48	25.23	24.69	24.79	24.92
FeO	13.15	13.23	14.34	13.92	13.86	13.48	14.28	13.34	13.81	15.09	13.29	16.24	13.97	13.84	13.42	13.75
MnO	0.18	0.16	0.16	0.16	0.17	0.16	0.17	0.16	0.16	0.19	0.14	0.19	0.17	0.16	0.17	0.17
NiO	0.20	0.19	0.19	0.20	0.21	0.21	0.23	0.20	0.20	0.20	0.21	0.20	0.21	0.20	0.24	0.21
MgO	17.53	17.58	16.91	17.24	17.22	17.46	16.77	17.15	17.30	16.19	17.48	16.87	16.71	17.19	17.78	17.16
CaO	0.00	0.01	0.00	0.01	0.01	0.01	0.00	0.01	0.04	0.01	0.01	0.01	0.01	0.03	0.01	0.01
Na <sub>2</sub> O	0.00	0.01	0.00	0.00	0.02	0.00	0.01	0.00	0.02	0.01	0.00	0.01	0.00	0.01	0.01	0.01
K <sub>2</sub> O	0.00	0.00	0.00	0.01	0.01	0.00	0.00	0.01	0.00	0.01	0.00	0.00	0.00	0.01	0.00	0.00
Si	0.001	0.001	0.000	0.000	0.001	0.000	0.001	0.001	0.001	0.000	0.011	0.000	0.000	0.001	0.001	0.001
Ti	0.001	0.001	0.001	0.000	0.001	0.001	0.001	0.001	0.001	0.001	0.001	0.001	0.001	0.001	0.001	0.001
Al	1.426	1.416	1.387	1.433	1.399	1.412	1.423	1.408	1.413	1.392	1.479	1.375	1.397	1.426	1.421	1.421
Cr	0.541	0.554	0.579	0.536	0.563	0.556	0.541	0.559	0.553	0.573	0.496	0.541	0.572	0.542	0.541	0.547
Fe <sup>2+</sup>	0.305	0.305	0.334	0.322	0.324	0.312	0.338	0.315	0.321	0.346	0.306	0.384	0.334	0.322	0.310	0.320
Mn	0.004	0.004	0.004	0.004	0.004	0.004	0.004	0.004	0.004	0.003	0.004	0.004	0.004	0.004	0.004	0.004
Ni	0.004	0.004	0.004	0.005	0.005	0.005	0.005	0.005	0.005	0.005	0.005	0.005	0.005	0.004	0.005	0.005
Mg	0.726	0.723	0.701	0.711	0.717	0.722	0.701	0.718	0.716	0.689	0.717	0.705	0.698	0.712	0.732	0.712
Ca	0.000	0.000	0.000	0.000	0.000	0.000	0.000	0.000	0.000	0.001	0.000	0.000	0.000	0.000	0.001	0.000
Na	0.000	0.001	0.000	0.000	0.001	0.000	0.001	0.001	0.000	0.001	0.000	0.000	0.000	0.000	0.001	0.000
K	0.000	0.000	0.000	0.000	0.000	0.000	0.000	0.000	0.000	0.000	0.000	0.000	0.000	0.000	0.000	0.000
Mg#	70.39	70.31	67.74	68.81	68.89	69.79	67.48	69.50	69.09	66.55	70.11	64.72	67.67	68.89	70.25	69.03
Cr/(Cr+Al)	27.51	28.12	29.45	27.22	28.71	28.26	27.56	28.41	28.11	29.15	25.09	28.25	29.07	27.55	27.79	27.79

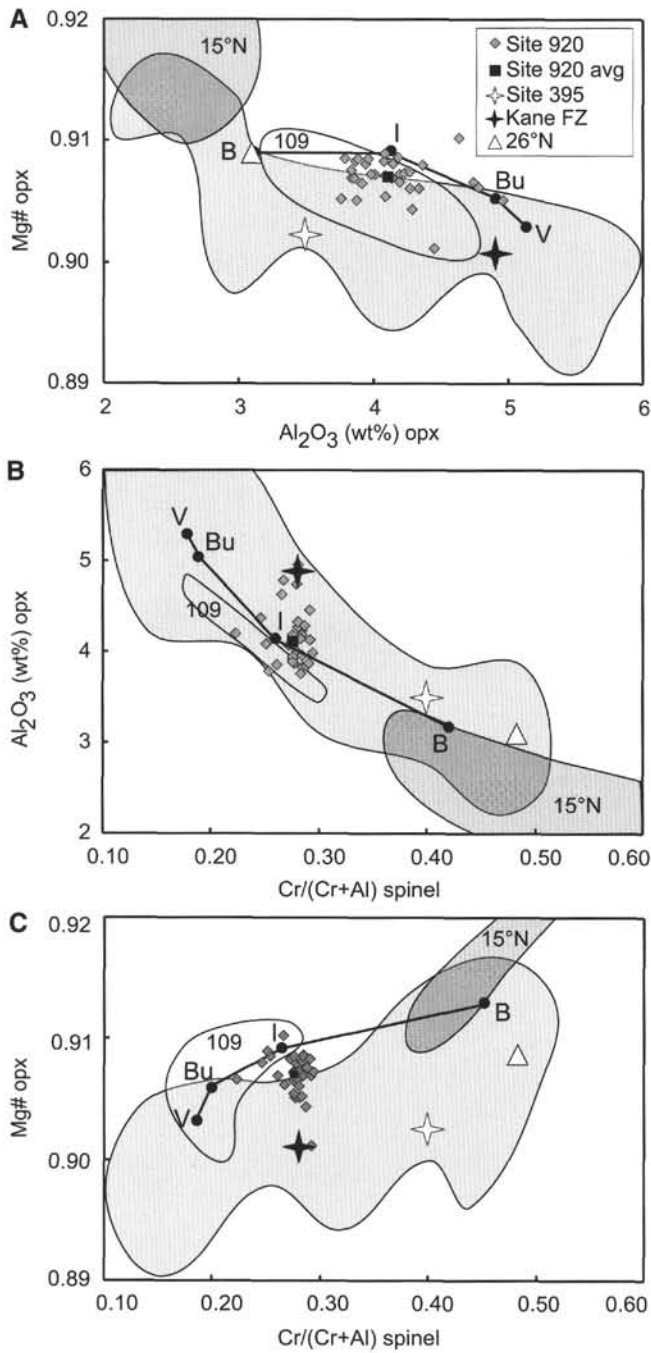


Figure 4. Site 920 orthopyroxene and spinel compositions plotted vs. the fields for North Atlantic peridotites of Michael and Bonatti (1985, shaded field). Site 395, Kane Fracture Zone (FZ), and 26°N are averages from the data of Michael and Bonatti (1985). V, Bu, I, and B are averaged compositions for Southwest Indian Ridge (SWIR) and American-Antarctic Ridge (AAR) fracture zone peridotites (V = Vulcan, Bu = Bullard, I = Islas Orcadas, B = Bouvet) from Dick et al. (1989). Field marked 109 is Hole 670A (ODP Leg 109) data from Juteau et al., 1990; field marked 15°N contains data from Cannat and Casey (1995) from Cape Verde Fracture Zone. A. Mg# in orthopyroxene vs. Al<sub>2</sub>O<sub>3</sub> in orthopyroxene. B. Al<sub>2</sub>O<sub>3</sub> in orthopyroxene vs. Cr# in spinel. C. Mg# in orthopyroxene vs. Cr# in spinel.

Table 7. Measured bulk-rock compositions for peridotites from Site 920.

Notes: Total excludes loss on ignition (LOI). All data are in weight percent (wt%). FeO\* = total Fe as FeO.

**Table 8.** Calculated bulk-rock compositions of spinel peridotite from Site 920.

Hole:	153-920B	153-920B	153-920B	153-920B	153-920B	153-920D	153-920D	153-920D	153-920D	153-920D	153-920D
Core, section:	13R-1	12R-5	12R-4	2R-1	10R-1	14R-3	12R-3	12R-3	5R-2	2R-2	14R-4
Interval (cm):	66–72	18–23	84–90	20–26	102–108	7–12	29–35	35–39	76–82	33–38	76–82
SiO <sub>2</sub>	43.51	39.58	42.65	45.44	43.01	43.98	42.68	43.24	41.11	42.58	44.95
TiO <sub>2</sub>	0.01	0.01	0.01	0.02	0.02	0.02	0.01	0.02	0.01	0.02	0.02
Al <sub>2</sub> O <sub>3</sub>	1.13	2.10	0.81	1.47	1.34	1.21	1.12	1.15	1.79	1.20	1.44
Cr <sub>2</sub> O <sub>3</sub>	0.35	1.16	0.23	0.43	0.54	0.36	0.43	0.40	0.80	0.55	0.37
FeO	8.43	9.20	8.46	7.88	8.74	8.48	8.58	8.63	8.78	9.14	8.09
MnO	0.12	0.13	0.13	0.14	0.14	0.13	0.13	0.12	0.13	0.13	0.13
NiO	0.31	0.36	0.32	0.30	0.33	0.30	0.34	0.30	0.33	0.33	0.29
MgO	46.57	48.18	45.11	45.39	47.11	45.01	46.22	46.37	46.59	47.66	44.56
CaO	0.60	0.26	1.67	0.31	0.28	1.41	0.54	0.78	0.81	0.33	1.12
Na <sub>2</sub> O	0.01	0.00	0.02	0.01	0.01	0.01	0.01	0.01	0.01	0.01	0.02
K <sub>2</sub> O	0.00	0.01	0.00	0.00	0.00	0.00	0.00	0.00	0.00	0.00	0.01

Hole:	153-920D	153-920D	153-920D	153-920D	153-920D	153-920D	Average	Vulcan	Bouvet	Bullard	Islas Orcadas
Core, section:	16R-3	22R-5	18R-2	22R-2	15R-5	22R-5					
Interval (cm):	64–70	11–116	35–41	69–73	14–22	3–9					
SiO <sub>2</sub>	43.32	43.44	44.09	40.65	42.11	45.41	43.12	43.65	42.97	43.74	43.67
TiO <sub>2</sub>	0.02	0.01	0.02	0.01	0.02	0.02	0.02	0.03	0.00	0.01	0.02
Al <sub>2</sub> O <sub>3</sub>	1.58	1.45	1.61	1.51	1.13	1.93	1.42	1.96	0.79	1.33	1.71
Cr <sub>2</sub> O <sub>3</sub>	0.62	0.53	0.49	0.77	0.46	0.49	0.53	0.36	0.25	0.33	0.31
FeO	8.39	8.35	8.43	8.79	8.61	7.85	8.51	8.43	8.27	8.25	8.31
MnO	0.13	0.14	0.14	0.13	0.13	0.14	0.13	0.15	0.12	0.15	0.13
NiO	0.32	0.32	0.32	0.35	0.34	0.28	0.32	0.22	0.25	0.25	0.21
MgO	46.07	45.72	45.26	46.95	47.17	41.88	45.89	42.87	45.83	44.29	43.61
CaO	1.06	0.78	0.53	0.91	0.75	1.27	0.80	1.99	0.76	1.45	1.41
Na <sub>2</sub> O	0.02	0.01	0.01	0.03	0.01	0.01	0.01	0.05	0.01	0.02	0.05
K <sub>2</sub> O	0.01	0.01	0.00	0.01	0.00	0.01	0.01	0.01	0.00	0.00	0.00

Notes: Compositions are calculated from analyzed mineral compositions from Tables 3 through 6, modal data from Table 2, and specific gravities of 3.34, 3.30, 3.30, and 4.30 g cm<sup>-3</sup>, respectively, for olivine, orthopyroxene, clinopyroxene, and spinel. Also tabled are the calculated average spinel peridotite compositions for the AAR and Southwest Indian Ridge peridotites from Dick (1989). All data are in weight percent (wt%).

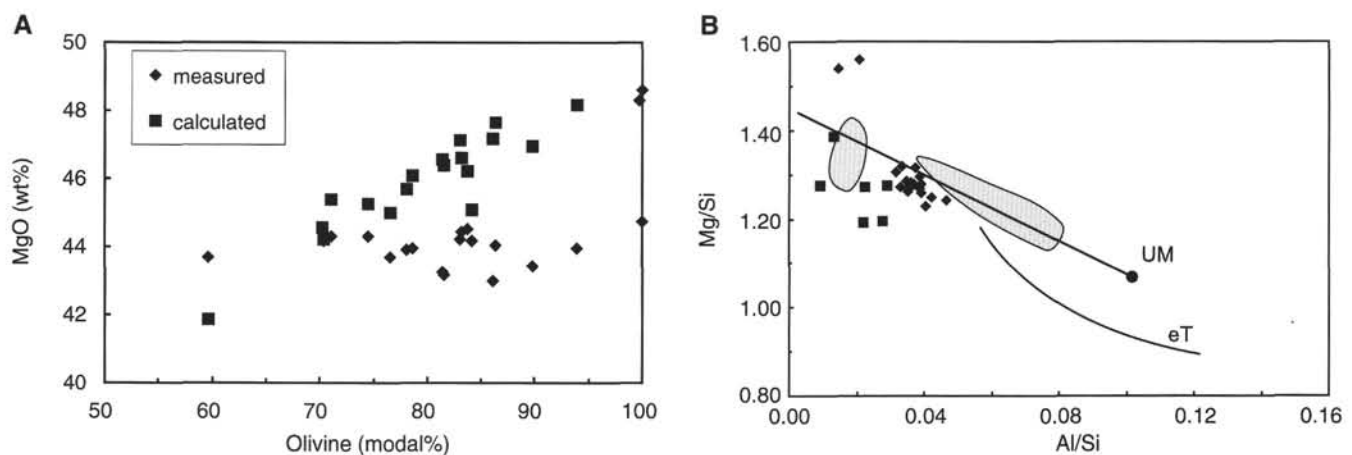


Figure 5. A. Comparison of measured and calculated MgO contents for Site 920 peridotites, showing the uniform measured composition and dependence of calculated composition on the modal estimate. B. Mg/Si vs. Al/Si (wt%) for Site 920 peridotites (diamonds). Data from Mid-Atlantic Ridge 43°N (squares) from Shibata and Thompson (1986). Shaded fields are from Trinity Ophiolite (Quick, 1981; Jacobsen et al., 1984; Gruau et al., 1991); curved line marked eT joins enriched Trinity Ophiolite data of Gruau et al. (1995); heavy line shows trend of melt depletion from Gruau et al. (1995); undepleted mantle (UM) composition is from Gruau et al. (1995), after Jacobsen et al. (1984) and Jagoutz et al. (1979).

**Table 9.** Trace-element ICP-MS analyses for peridotites from Site 920.

Hole:	153-920B	153-920D	153-920D	153-920D	153-920D						
Core, section:	13R-1	12R-5	12R-4	2R-1	12R-1	10R-1	7R-1	14R-3	12R-3	12R-5	12R-3
Interval (cm):	66–72	18–23	84–90	20–26	132–135	102–108	131–135	7–12	29–35	36–43	35–39
Y	0.6782	0.5551	0.5160	0.4896	0.0518	0.4405	0.4773	0.5669	0.5188	0.0735	0.7178
Zr	0.0605	0.0301	0.0710	0.0519	0.1962	0.0558	0.0474	0.1115	0.0394	0.0845	0.1663
Nb	0.0085	0.0040	0.0085	0.0018	0.0035	0.0076	0.0052	0.0072	0.0037	0.0031	0.0099
Ta	0.0090	0.0021	0.0047	0.0019	0.0100	0.0008	0.0011	0.0027	0.0000	0.0076	0.0000
La	0.0000	0.0000	0.0286	0.0000	0.0005	0.0007	0.0040	0.0129	0.0000	0.0000	0.0229
Ce	0.0000	0.0000	0.1062	0.0000	0.0027	0.0080	0.0088	0.0246	0.0000	0.0000	0.0515
Pr	0.0004	0.0000	0.0145	0.0004	0.0009	0.0016	0.0019	0.0040	0.0008	0.0005	0.0071
Nd	0.0021	0.0014	0.0515	0.0008	0.0038	0.0079	0.0074	0.0164	0.0044	0.0020	0.0309
Sm	0.0116	0.0072	0.0152	0.0105	0.0059	0.0077	0.0096	0.0112	0.0099	0.0042	0.0154
Eu	0.0056	0.0048	0.0047	0.0063	0.0213	0.0118	0.0091	0.0049	0.0051	0.0025	0.0061
Gd	0.0365	0.0291	0.0316	0.0251	0.0072	0.0219	0.0235	0.0334	0.0307	0.0073	0.0367
Tb	0.0070	0.0046	0.0053	0.0036	0.0000	0.0024	0.0032	0.0047	0.0043	0.0000	0.0064
Dy	0.0867	0.0689	0.0657	0.0656	0.0062	0.0565	0.0554	0.0695	0.0698	0.0088	0.0887
Ho	0.0237	0.0199	0.0187	0.0176	0.0016	0.0150	0.0165	0.0200	0.0186	0.0026	0.0256
Er	0.0881	0.0720	0.0694	0.0657	0.0091	0.0569	0.0629	0.0728	0.0662	0.0112	0.0899
Tm	0.0149	0.0127	0.0120	0.0112	0.0020	0.0108	0.0116	0.0127	0.0108	0.0026	0.0151
Yb	0.1151	0.0992	0.0948	0.0863	0.0196	0.0825	0.0884	0.0979	0.0826	0.0215	0.1224
Lu	0.0192	0.0179	0.0177	0.0160	0.0048	0.0148	0.0165	0.0180	0.0148	0.0046	0.0213
Hf	0.0060	0.0047	0.0058	0.0057	0.0073	0.0052	0.0060	0.0073	0.0051	0.0035	0.0073
Li	1.2461	0.5189	0.6542	0.2950	0.0237	1.0384	0.5951	0.8878	0.2797	0.0084	0.7486
Be	0.0000	0.0000	0.0006	0.0000	0.0637	0.0135	0.0030	0.0000	0.0000	0.0001	0.0076
Sc	17.5716	17.6089	18.1989	16.7724	7.3434	16.7505	14.6480	17.5275	13.9819	6.4896	20.8737
V	63.2571	55.7906	61.8518	56.1756	13.8474	54.9105	56.2365	58.6005	49.4141	24.1894	76.1964
Co	117.7581	119.7284	135.7229	136.1796	163.4525	128.9862	129.9715	128.4725	132.7437	159.1360	122.3752
Cu	19.2535	15.6425	20.0479	3.9213	10.1246	16.7465	21.8057	20.0057	38.3778	7.3632	21.6768
Zn	35.4819	34.1517	43.1901	34.7233	36.9144	33.4928	37.4260	39.5542	40.5372	48.0528	41.5169
Ga	1.4654	1.2830	1.6321	1.4563	0.9304	1.6579	1.5820	1.5058	1.3820	1.2864	1.8955
Rb	0.0083	0.0056	0.0149	0.0581	0.0121	0.0161	0.0270	0.0544	0.0070	0.0067	0.0951
Sr	2.0979	2.2675	2.4288	2.8381	2.4650	2.6572	2.7675	2.2781	3.2225	2.5774	3.3483
Cs	0.0012	0.0014	0.0004	0.0023	0.0019	0.0015	0.0016	0.0023	0.0009	0.0011	0.0023
Ba	0.1285	0.0431	0.0781	0.2136	0.3393	0.1319	0.1465	0.3971	0.0651	0.7019	0.3867
Pb	0.0000	0.0000	0.0000	0.0000	0.0000	0.0000	0.0152	0.0000	0.0000	0.0000	0.0000
Bi	0.0044	0.0035	0.0032	0.0030	0.0034	0.0035	0.0032	0.0029	0.0028	0.0035	0.0000
Th	0.0021	0.0009	0.0026	0.0010	0.0040	0.0321	0.0020	0.0136	0.0011	0.0019	0.0194
U	0.0000	0.0000	0.0000	0.0000	0.0000	0.0000	0.0016	0.0121	0.0000	0.0000	0.0023

Notes: All data are reported as parts per million (ppm) normalized to water-free compositions using measured loss on ignition.

**Table 9 (continued).**

Hole:	153-920D										
Core, section:	5R-2	2R-2	14R-4	15R-1	16R-3	22R-5	18R-2	22R-2	15R-5	22R-5	
Interval (cm):	76–82	33–38	76–82	8–15	64–70	113–116	35–41	69–73	14–22	3–9	
Y	0.5496	0.5715	0.4576	0.5383	0.3649	0.5882	0.5817	0.4810	0.5338	0.5536	
Zr	0.0654	0.0671	0.1011	0.0483	0.0808	0.0858	0.1824	0.0457	0.0446	0.0446	
Nb	0.0100	0.0033	0.0140	0.0043	0.0033	0.0051	0.0104	0.0030	0.0025	0.0072	
Ta	0.0135	0.0022	0.0010	0.0244	0.0081	0.0081	0.0063	0.0063	0.0012	0.0077	
La	0.0087	0.0084	0.0280	0.0028	0.0000	0.0000	0.0009	0.0000	0.0000	0.0065	
Ce	0.0079	0.0151	0.0532	0.0048	0.0005	0.0000	0.0013	0.0000	0.0000	0.0064	
Pr	0.0012	0.0016	0.0044	0.0009	0.0007	0.0006	0.0009	0.0006	0.0004	0.0006	
Nd	0.0060	0.0099	0.0133	0.0050	0.0049	0.0046	0.0097	0.0028	0.0053	0.0068	
Sm	0.0136	0.0107	0.0069	0.0119	0.0049	0.0142	0.0158	0.0093	0.0100	0.0131	
Eu	0.0088	0.0091	0.0041	0.0048	0.0042	0.0058	0.0046	0.0043	0.0054	0.0045	
Gd	0.0308	0.0302	0.0260	0.0336	0.0205	0.0361	0.0325	0.0260	0.0291	0.0290	
Tb	0.0056	0.0045	0.0027	0.0057	0.0014	0.0052	0.0051	0.0037	0.0043	0.0053	
Dy	0.0740	0.0727	0.0555	0.0750	0.0449	0.0768	0.0791	0.0614	0.0695	0.0738	
Ho	0.0200	0.0210	0.0153	0.0202	0.0135	0.0210	0.0210	0.0176	0.0198	0.0210	
Er	0.0740	0.0801	0.0587	0.0714	0.0508	0.0772	0.0799	0.0657	0.0736	0.0747	
Tm	0.0125	0.0136	0.0102	0.0119	0.0092	0.0125	0.0137	0.0114	0.0129	0.0135	
Yb	0.1002	0.1083	0.0809	0.0925	0.0735	0.0992	0.0999	0.0915	0.1008	0.1007	
Lu	0.0192	0.0195	0.0148	0.0169	0.0145	0.0185	0.0183	0.0169	0.0184	0.0193	
Hf	0.0071	0.0059	0.0061	0.0057	0.0054	0.0073	0.0093	0.0053	0.0057	0.0066	
Li	0.5945	0.6185	0.9752	0.8842	0.7683	1.4402	1.0323	1.0254	1.3759	0.9101	
Be	0.0350	0.0207	0.0274	0.0075	0.0111	0.0186	0.0193	0.0006	0.0213	0.0164	
Sc	16.3375	16.6231	13.5551	14.6988	12.9992	14.1750	18.0326	12.9121	15.5658	16.1116	
V	60.8328	62.0034	51.6945	53.6254	51.9217	52.6734	55.4993	49.8900	59.6443	60.8421	
Co	120.0454	116.4746	118.7040	122.5707	113.5449	116.4241	124.9309	109.8979	114.4834	120.1780	
Cu	7.6644	29.6515	11.0928	15.7392	15.9965	21.9338	32.5526	24.9444	13.7693	18.8644	
Zn	45.7870	35.8348	38.8381	35.2789	33.6638	30.1757	37.4137	38.5484	36.5478	42.6190	
Ga	1.6333	1.6441	1.4565	1.3299	1.3161	1.5501	1.3999	1.4113	1.4993	1.6195	
Rb	0.0420	0.1096	0.0187	0.0117	0.0158	0.0318	0.1011	0.0203	0.0285	0.0354	
Sr	97.9064	8.5095	2.7186	2.8993	2.2667	3.2088	3.4737	2.3083	3.4586	2.9349	
Cs	0.0030	0.0066	0.0013	0.0014	0.0025	0.0022	0.0020	0.0026	0.0020	0.0008	
Ba	0.2001	0.3864	0.1779	0.2961	0.2976	0.3051	0.4172	0.3678	0.2752	0.1594	
Pb	0.0000	0.2695	0.0000	0.0000	0.0000	0.0000	0.0000	0.0000	0.0000	0.0000	
Bi	0.0000	0.0012	0.0009	0.0000	0.0000	0.0000	0.0024	0.0000	0.0000	0.0000	
Th	0.0022	0.0003	0.0058	0.0009	0.0120	0.0022	0.0085	0.0015	0.0017	0.0020	
U	0.0049	0.0253	0.0026	0.0003	0.0003	0.0000	0.0000	0.0000	0.0000	0.0000	

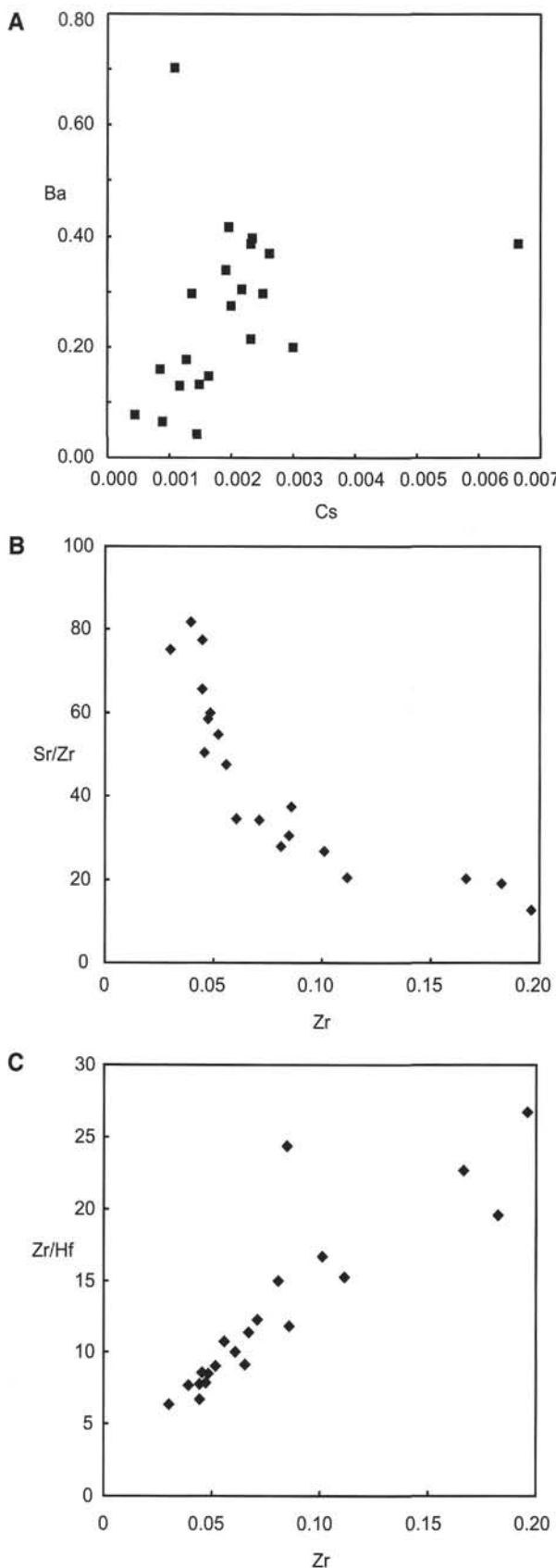


Figure 6. Trace-element compositions in Site 920 peridotites (in ppm) showing (A) good correlation between Cs and Ba, suggestive of seawater alteration; (B) unusual correlation between Sr/Zr and Zr; and (C) decreasing Zr/Hf with decreasing Zr. See text for discussion.

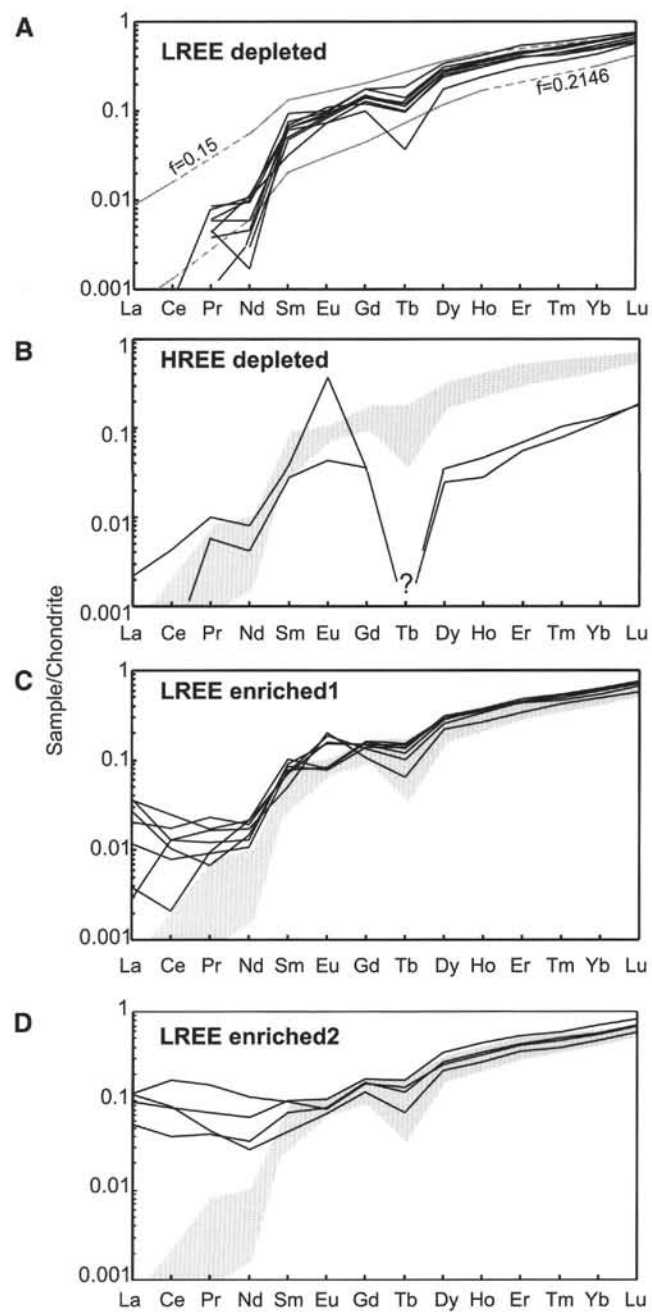


Figure 7. Subgroups of Site 920 peridotites on the basis of their chondrite-normalized (Sun and McDonough, 1989) REE patterns. Lines marked  $f = 0.15$  and  $f = 0.2146$  on (A) are residual compositions for 15% and 21.46% fractional melting of fertile spinel peridotite from Ewart and Hawkesworth (1987). The range corresponds to less than 3 modal% clinopyroxene at  $f = 0.15$  to clinopyroxene exhaustion at  $f = 0.2146$ . Shaded areas on (B), (C), and (D) indicate the range for LREE-depleted patterns from A. Subdivisions are discussed in the text.

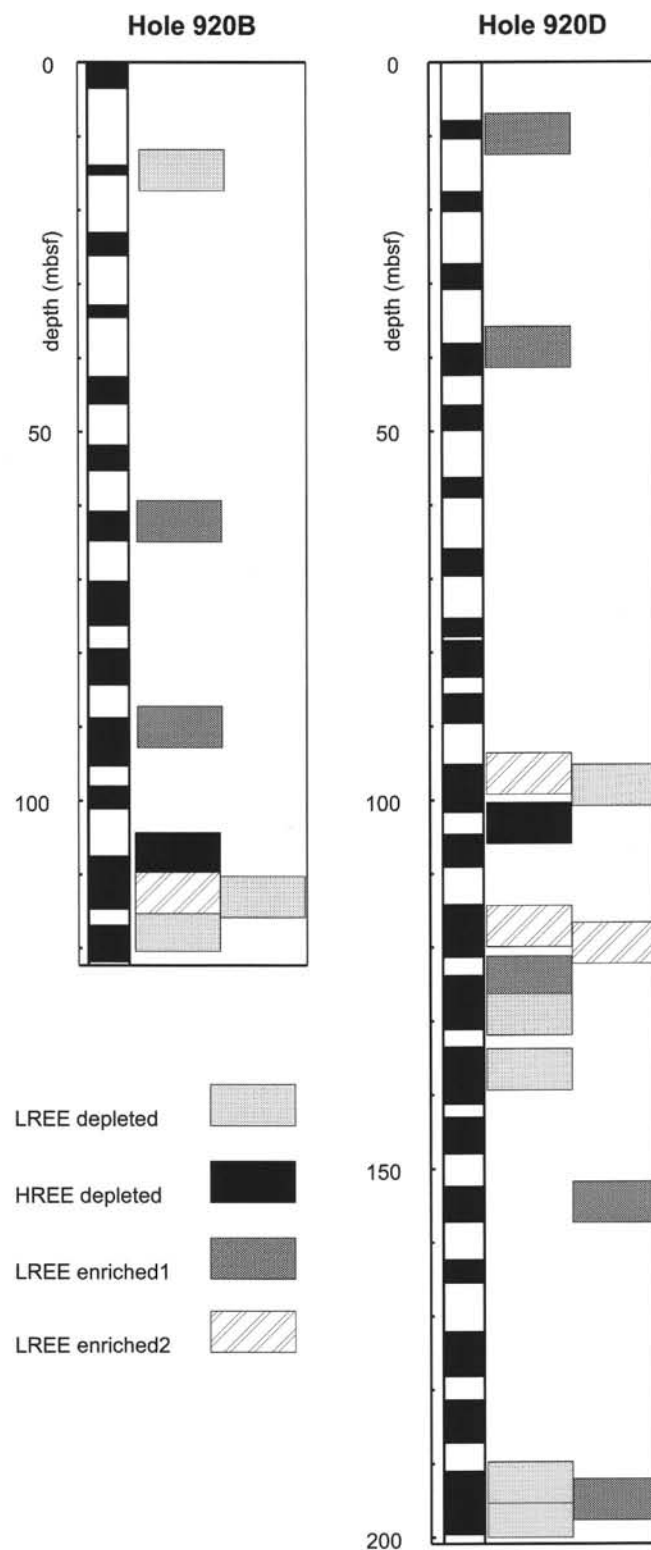


Figure 8. Distribution of individual samples in Site 920 drill holes based on their REE patterns, as defined in the text.